Rheinisch-Westfälische Technische Hochschule Aachen (RWTH)

Investigation of a dipole magnet for spin manipulation at EDM at COSY

Untersuchung eines Dipolmagneten zur Spinmanipulation im Rahmen des EDM am COSY-Projekts

von
Martin Rongen

Bachelorarbeit in Physik

vorgelegt der

Fakultät für Mathematik, Informatik und Naturwissenschaften
der RWTH Aachen

im August 2012

angefertigt am Dritten Physikalischen Institut B

bei

Professor Doktor Jörg Pretz

August 22, 2012

Eidesstattliche Erklärung:

Ich versichere, dass ich die vorgelegte Arbeit selbstständig verfasst
und keine anderen als die angebenen Quellen und Hilfsmittel benutzt
sowie Zitate kenntlich gemacht habe.

Affirmation:

I affirm that I wrote the present thesis without any inadmissible help by a third party and without using any other means than indicated.
Thoughts that were taken directly or indirectly from other sources are indicated as such.

Aachen, den

Acknowledgement:

I would like to gratefully and sincerely thank Prof. Jörg Pretz for his mentorship and the countless opportunities offered during the last semester.
I would also like to thank PD. Andreas Lehrach and Ralf Gebel for their patience in numerous discussions and the access to the local lab-space.

Contents

1 Motivation

Over the past decades the Standard Model of particle physics (SM) has been validated to unprecedented accuracy and is now the foundation for our understanding of the universe. Nevertheless it currently fails at explaining the baryogenesis, i.e. the origin of the matter-antimatter asymmetry, which enables our very existence [1, p7].

In 1967 Andrei Sakharov identified a strong violation of the charge- and parity-reversal symmetries (CP violation) as one requirement for this process [2].
Although CP violation is not strictly forbidden within the SM (it can be parametrized by the phase in the Cabibbo-Kobayashi-Maskawa matrix, if the number of quark families is bigger than two), the resulting baryon asymmetry as deduced from the SM

$$\eta = \frac{n_B - n_{\bar{B}}}{n_\gamma} \approx 10^{-18} \tag{1.1}$$

is eight orders of magnitude smaller than the value measured by the COBE and WMAP satellites [1, 3]. Experimentally CP violation has been discovered in 1964 in the kaon decay processes [4]. It is now being studied in meson and B-decays, for example at LHCb and in the neutrino flavour oscillation.

The existence of an electric dipole moment (EDM) alongside the well-known magnetic dipole moment (spin) would be time and parity-reversal violating [1]. This can be easily understood in a semi-classical model, in which the spin can be thought as the magnetic dipole moment generated by a circular current. In the same model the EDM is the vector between two opposite and separated charges along the axis of spin. Under time-reversal the current flow and thus the MDM is reversed while the charge distribution (EDM) stays unaffected. In the case of parity-reversal the opposite is true (see also figure 1.1).

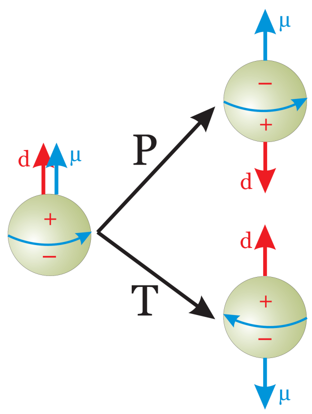

Figure 1.1: PT violation visualised ©Andreas Knecht

Under the assumption of CPT-invariance time-reversal violation implies CP violation. Thus the EDM, if it exists, is CP violating.

The SM expectation for the EDM of nucleons is between 10^{-33} to 10^{-31} $\mathrm{e \cdot cm}$. Equivalent estimations of EDM-strength can be deduced from extensions of the SM (see figure 1.2), while the measured baryon numbers yield an expectation of up to 10^{-25} $\mathrm{e \cdot cm}$ [1].

Over the past five decades numerous experiments have set ever decreasing upper limits on the neutron EDM (see figure 1.2). The current record (as of 2012) is held by the university of Sussex at $2.9 \cdot 10^{-26}$ $\mathrm{e \cdot cm}$. To put this value into a human perspective consider the following: If we were to expand a neutron (around 1 fm) to the size of the earth (around 13,000 km), the current EDM limit would equal a separation of two electrons by less than a quarter of a millimeter. The accuracy on the neutron EDM is fundamentally limited by the lifetime of free neutrons and the availability of ultra-cold neutrons [5].

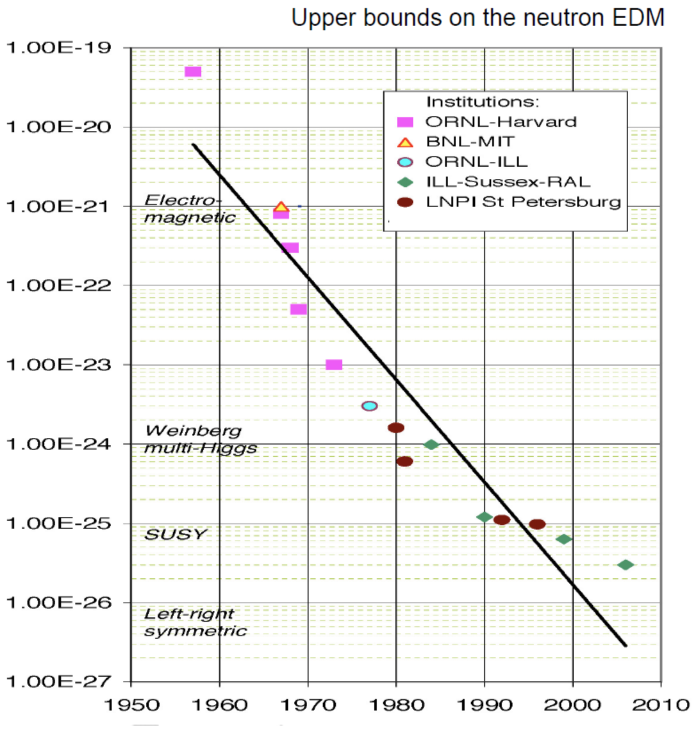

Figure 1.2: Upper limit on n-EDM vs. time [6]

It has recently been proposed to extend the EDM search onto charged baryons, namely protons, deuteron and Helium-3. For charged particles particle-trap experiments, as used for neutrons, can no longer be employed because large electro-magnetic fields have to be applied. Instead the particles can be stored, manipulated and analysed within a particle accelerator. At the end of 2011 the JEDI (Jülich Electric Dipole moment Investigations) collaboration was created to work towards such an experiment at the Jülich polarized hadron accelerator COSY or a subsequent machine. Should these new experiments reach the design criteria it will then be possible to increase the sensitivity to around 10^{-29} $\mathrm{e \cdot cm}$ [1].

The measurements on deuteron and helion (Helium-3 nucleus) will gain mayor importance, should a non-vanishing EDM be found, as only the combination of results allows to unfold the underlying physics and extract the source of the charge separation [7].

This thesis deals with the evaluation of a new dipole magnet, which is supposed to be used for spin manipulation in the first of three proposed steps towards a final EDM experiment at Forschungszentum Juelich. Its main purposes will be to evaluate false spin rotations induced for example by fringe fields and to evaluate the effect of different waveform on spin-coherence-time [1, p12]. In the following the needed accelerator and spin-dynamics physics will be summarized to then briefly present the proposed experimental method to measure EDMs in storage ring. From this arises the need for the new dipole magnet. The integral field and other associated characteristics of the newly built device are then deduced from measurements and simulation and will be compared to data recorded during the May 2012 JEDI beamtime at the COSY accelerator facility.

2 Theoretical background

2.1 Accelerator basics

A particle accelerator is a device to specifically manipulate the motion of charged subatomic particles. Today devices like this are used for a wide variety of applications, spanning the fundamental, material, medical and even energy sciences. The acceleration of a charged particle in electro-magnetic fields is given by the Lorentz force

$$\vec{F} = q(\vec{E} + \vec{v} \times \vec{B}). \tag{2.1}$$

In the following basic concepts of different accelerator types and some fundamentals of linear beam optics are introduced to aid the understanding of the later presented spin dynamics.

2.1.1 Linear accelerators

The first accelerators in existence simply used a static electric field for acceleration. In this approach the maximum energy is severely limited (several MeV) by the maximum voltage that can be technically supplied. The breakthrough to higher energies was only possible with the availability of high frequency (RF) amplifiers. In the original design by Ising and Widerøe (theoretical: 1925, experimental: 1929 [8, p12]) the particles are accelerated in gaps between grounded drift tubes. The drift tube lengths and the RF have to be matched, so that the particles always see an accelerating potential when leaving the drift tubes. In theory the energy of such a device is only limited by its length.

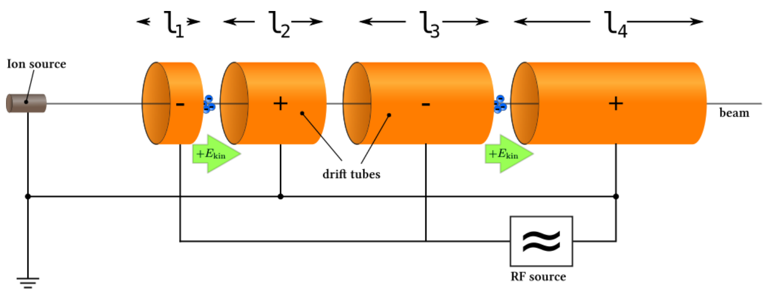

Figure 2.1: Linear particle accelerator

2.1.2 Circular accelerators

The existence of RF cavities also made it possible to cut down the size of accelerators by building circular devices, so that the beam particles pass the same set of manipulating fields periodically. The two most common designs are:

Cyclotron (see figure 2.2a)

The particles get injected into the center of a constant magnetic field transverse to their momentum direction and travel in so called 'DEEs' that shield the particles from electric fields for half a revolution each. The frequency of a driving electric field between the dees is chosen so that the particle get accelerated each time they travel from dee to dee. The beam spirals to the outside of the cyclotron as the energy increases and is then extracted via a kicker electrode.

In a purely classical situation the revolution frequency (cyclotron frequency) is constant and is given by an equilibrium between the Lorentz force and the centripetally force:

$$\frac{mv^2}{r} = qvB \qquad\qquad f = \frac{v}{2\pi r} = \frac{qB}{2\pi m}. \tag{2.2}$$

The maximum energy of a cyclotron is (for heavy particles) mainly limited by relativistic effects, which are partially dealt with in so called synchro-cyclotrons [8, p17].

Synchrotron (see figure 2.2b)

In contrast to a cyclotron the beam path within a synchrotron is fixed to a beam pipe. This allows for easy installation of experiments, higher order magnets and diagnostic tools. In order to achieve this the guiding magnetic field has to be increased as the beam energy increases. Synchrotrons usually have a limited operating range in energy, so that pre-accelerators are needed to provide the initial beam.

For heavy particles the maximum beam energy is only limited by the product of the magnetic field and the ring diameter (see equation 2.2). Light particles quickly start to lose energy due to synchrotron radiation ($\Delta E \propto E^4/(m^4 R)$ [8, p38]), which severely limits their upper energy, but gives rise to a new research area which utilises the produced light.

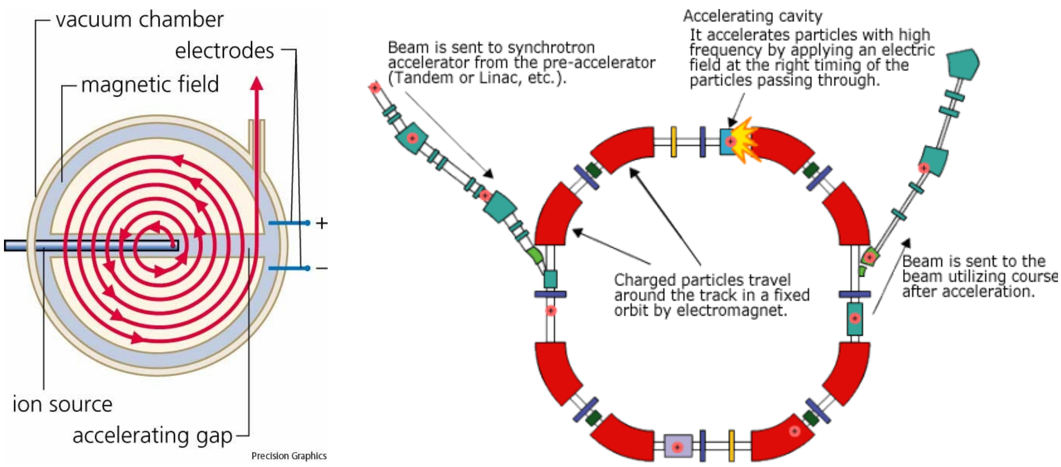

(a) Cyclotron [9]

(b) Synchrotron [10]

Figure 2.2: Circular accelerator concepts

2.1.3 Linear beam optics of circular accelerators

Up to now we have only considered the dipole fields needed to bend the particles along the desired beam path. In a real beam the particles trajectories are always slightly diverging, so that the beam quickly spreads out and eventually gets lost at the beampipe [8, p51]. Additional elements are needed to guide these particles back onto the desired path.

The trajectory of each particle in the beam is given by the electro-magnetic elements along the beam pipe. For the following discussion we want to consider only magnetic fields, which is the most common case, and introduce the co-moving coordinate system K(x,y,s). The origin sits on any point on an ideal beam trajectory called orbit [8, p54], around which the particles oscillate and moves forth with the orbit angle θ. The axis s points along the beam momentum, while x and y denote the radial (horizontal) and vertical directions.

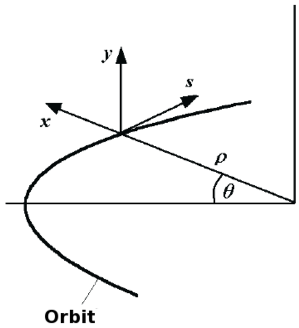

Figure 2.3: Accelerator coordinate system [11]

Only transverse magnetic fields act on the primarily longitudinally moving particles and induce transverse motion. The relevant particles stay close to the orbit compared to the overall radius, so that the for example vertical magnetic field B_y, inducing motion in the horizontal direction, can be expressed by a Taylor series:

$$\begin{aligned} \frac{q}{p}B_y(x) &= \frac{q}{p}B_{y0} + \frac{q}{p}\frac{\partial B_y}{\partial x}x + \frac{1}{2}\frac{q}{p}\frac{\partial^2 B_y}{\partial x^2}x^2 + ... \\ &= \underbrace{\frac{1}{R}}_{\text{Dipole}} + \underbrace{kx}_{\text{Quadrupole}} + \underbrace{\frac{1}{2}mx^2}_{\text{Sextupole}} + ... \end{aligned} \tag{2.3}$$

The values have been rescaled by the momentum in order to archive energies independent field strengths (1/R, m, k). Each term can be associated with a magnetic multipole and has a specific primary action on the beam. Dipole fields keep the beam on its circular motion. Quadrupole fields focus the particles around the orbit. And sextupole fields correct for chromatic effect, this is the slightly different focussing strength of particles which are not at the nominal momentum. In modern accelerators each multipole is being realised by an independent set of magnets, although it is also easily feasible to superimpose different multipoles in one component, to allow for a great flexibility in settings [8, 3.1]. In the following we do not want to consider chromatic and higher order effects, so that the only remaining multipoles to consider are dipoles and quadrupoles.

Only considering transverse fields to this order one can, for a perfect beam (i.e. $\Delta p/p = 0$), deduce the following set of linear, homogeneous differential equations from the Lorentz force and the above defined coordinate system alone [8, p58]:

$$x''(s) + \left(\frac{1}{R^2(s)} - k_x(s)\right) x(s) = 0, \tag{2.4}$$

$$y''(s) + k_y(s) y(s) = 0. \tag{2.5}$$

R(s) and k(s) are the local bending radii and quadrupol focussing strength, which repeat periodically with the accelerator circumference. The set of differential equations describes the so called betatron motion, this is the motion in the transverse plane. Each equation is basically a harmonic oscillator with an orbit position dependent spring factor (Hill equation) for which the general solution is given by the Floquet theorem [11, p12] to be

$$f_\beta(s) = \sqrt{\epsilon_{x/y}\beta(s)} \cdot \cos\left(\Psi(s) + \Phi\right). \tag{2.6}$$

This betatron oscillation function f_β cannot only be utilised to describe the motion of single particles but also (when choosing $\epsilon_{x/y}$ and $\beta(s)$ accordingly) describes the position dependent 1σ transverse beam size along the beam pipe [8, 88]. The emittance $\epsilon_{x/y}$ can for our purposes be considered as a constant value and is a measure of the beam quality. The local betatron value ($\beta(s)$) is a result of the arrangement of magnets in the accelerator (lattice) and is usually calculated with a matrix technique in which each magnet in the machine is represented [8, 3.11]. Figure 2.4 shows an example of a β function for the COSY lattice.

For very simple devices the betatron function can be analytically deduced from the differential equation [8, p89]

$$\sqrt{\beta(s)} - \frac{1}{\sqrt{\beta(s)}^3} - k(s) \cdot \sqrt{\beta(s)} = 0. \tag{2.7}$$

The phase of the betatron motion is given by substituting the ansatz 2.6 back into 2.5:

$$\Psi(s) = \int_0^s \frac{ds'}{\beta(s')} + \Psi_0. \tag{2.8}$$

The number of betatron oscillations in one direction during one revolution of the beam is called betatron tune ν and is directly given by the advance in phase during this time:

$$\nu = \frac{\Psi(s + 2\pi r) - \Psi(s)}{2\pi} = \frac{1}{2\pi} \oint \frac{ds}{\beta(s)}. \tag{2.9}$$

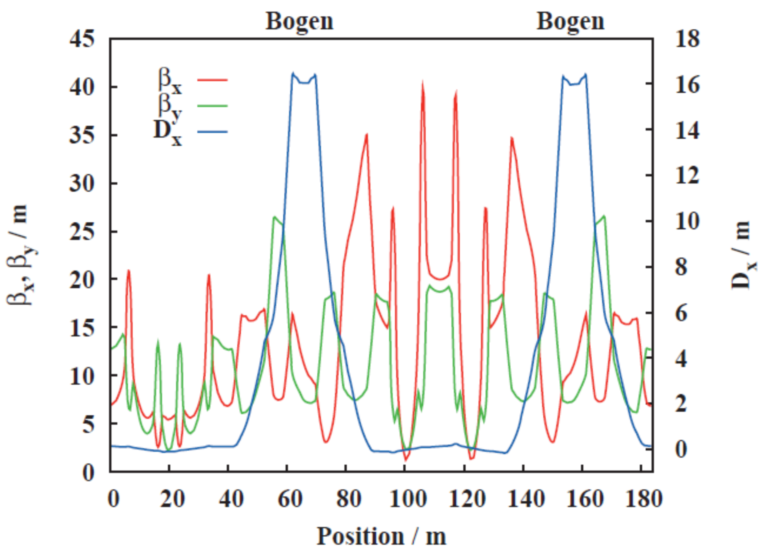

Figure 2.4: Example betatron function of the COSY lattice [11]

2.1.4 Optical resonances

The magnetic fields and so the forces on the beam particles act periodically with each revolution. The placement and the field of each magnet is never ideal. This can, under certain circumstances, lead to a resonance between the betatron oscillations and the lattice which dramatically increases the beam size. Detailed calculations on this topic are lengthy and basically follow the above train of thought [8, p118ff]. In order to understand the concept we can instead qualitatively discuss a simple example.

Consider an ideal accelerator with only a single slightly missplaced dipole magnet. Each time the beam passes this spot the beam particle suffers a slight angular kick. They are not directly lost as following quadrupole fields force them back close to the orbit, but in the following sections the amplitude of the betatron oscillation is increased. If the particles reach the defective dipole with varying phases of the betatron oscillation, the effect of the angular kicks will average out over a number of turns. But if the phase is always the same the kicks will add up resonantly and the beam will eventually be lost. Hence we see that integer tune are to be avoided.

Higher order field defects lead to higher order resonances, which accordingly decrease in strength. So in order to avoid quadrupole/sextupole resonances multiples of 1/2 / 1/3 have to be avoided as tune [8, p125f].

2.2 Spin-dynamics

While the amplitude of the magnetic moment of any particle is an intrinsic property, the direction of this vector can be manipulated by external fields. The behaviour of individual particle spin and of the beam polarisation as a whole, is a function of the lattice as described below. The polarisation P along an axis $\vec{n}$ is the sum of the scalar products of all particles spins with this axis:

$$P = \sum_i \vec{S}_i \cdot \hat{\vec{n}}. \tag{2.10}$$

2.2.1 Thomas-BMT equation

The force (torque) on a magnetic moment at rest due to a magnetic field in the rest frame B^* is given by [11, p35f]

$$\frac{d\vec{S}}{dt} = \vec{\mu} \times \vec{B}^*. \tag{2.11}$$

Where the spin $\vec{S}$ and the magnetic moment $\vec{\mu}$ are related by

$$\vec{\mu} = g\frac{q}{2m}\vec{S}. \tag{2.12}$$

For a Dirac particle g is given to be 2, due to not point-like charge-distributions the actual values differ from this by the gyromagnetic anomaly G:

$$G = \frac{g-2}{2} = \begin{cases} 0.00116, & \text{for the electron} \\ 1.79284, & \text{for the proton} \\ -0.14298, & \text{for the deuteron} \end{cases} \tag{2.13}$$

The torque on a resting EDM, which as magnetic and electric moments always point in the same direction also effect the spin-axis, in an electric field is given by the Lorentz force [12, 3]

$$\frac{d\vec{S}}{dt} = \vec{d} \times \vec{E}^*. \tag{2.14}$$

In the resulting sum the fields have to be transformed from the rest frame of the particles to the lab frame ($\vec{B}^* \rightarrow \vec{B}$, $\vec{E}^* \rightarrow \vec{E}$) in order to see the effects of the lattice. The resulting rotational movement with the angular frequency Ω is given by the so called Thomas-BMT (Bargmann, Michel and Telegdi) formula [1, 12, 11, 13]:

$$\frac{d\vec{S}}{dt} = \vec{S} \times (\vec{\Omega}_{MDM} + \vec{\Omega}_{EDM}) \tag{2.15}$$

$$\vec{\Omega}_{MDM} = \frac{e}{m\gamma} \cdot \left[(1+\gamma G)\vec{B}_{\perp} + (1+G)\vec{B}_{\parallel} - \left(\gamma G + \frac{\gamma}{1+\gamma}\right)\frac{\vec{\beta}\times\vec{E}}{c}\right] \tag{2.16}$$

$$\vec{\Omega}_{EDM} = -d\frac{c}{S\hbar} \cdot \left(\frac{\vec{E}}{c} + \vec{\beta}\times\vec{B}\right) \tag{2.17}$$

Where the magnetic field has been split up into components parallel and perpendicular to the momentum.

This expression is structurally similar to the Lorentz force that governs the particles movement ($\Omega = eB/m_{\gamma}$). In an ideal accelerator, only consisting of dipole magnets the spin thus rotates $(1 + \gamma G)$ times during one rotation of the beam. The number of rotations of the spin in the rest frame of the particle is commonly called spin tune $\nu_s = \gamma G$. This value derived only from the holding dipole fields is usually accurate within the error of measurement even for a referance particle in a real machine. In the same model the axis of rotation is fixed along the vertical axis. This axis is called invariant spin axis, as only polarisation along this axis is preserved [11, 4.2.2]. For a real accelerator the invariant spin axis might be slightly different and will also dependent on the position along the orbit.

2.2.2 Spin-resonances

Unexpected fields in respect to a reference particle on the calculated orbit kick the spin orientation of off-orbit particles away from the invariant spin axis just as they kick the momentum axis each time the beam passes. We can thus follow the same principle argumentation as in section 2.1.4 to understand the resonance conditions that lead to a loss of polarisation in respect to the invariant spin axis [11, 13, p11f, p30].

Imperfection resonances:

If the phase of the spin rotation is the same each time a field defect (i.e. due to positioning errors) is passed the kicks add up resonant. This condition can be translated to an integer spin tune.

$$\nu_s = \gamma G = k \in \mathbb{N} \tag{2.18}$$

Intrinsic resonances:

The particles undergoing betatron oscillations will see additional (horizontal) fields due to the focussing quadrupoles. Their kicks add up when spin oscillation and betatron motion are in phase.

$$\nu_s = \gamma G = k \pm \nu_y \tag{2.19}$$

Higher order resonances
: due to for example the horizontal betatron oscillation or the synchrotron motion of the beam.

There are two common methods to avoid polarisation losses when approaching a resonance during acceleration. One involves adiabatically crossing the resonance, which results in a reversed polarisation (see section 2.2.3). The other method uses fast quadrupoles that can temporally move the tune and thus shift the spin resonance condition.

2.2.3 Spin manipulation with RF-B-fields

Artificial spin-resonances can be introduced into the machine, so that a polarisation along an arbitrary axis can be produced. If the RF-frequency of the dedicated magnet matches the primary resonance condition the spin will rotate around an axis along the magnetic field of the magnet. The rotational angle per revolution on resonance can be deduced from the BMT-equation 2.17, by basically multiplying by the revolution period and considering only the phases when the magnet acts on the spin, to be [11, 14]

$$\epsilon_{BDL} = \left\langle \frac{1}{4\pi} \oint [\underbrace{(1+\gamma G)\cdot \frac{B_\perp}{B}}_{\text{dipole}} + \underbrace{(1+G)\cdot \frac{B_\parallel}{B}}_{\text{solenoid}}] e^{i\nu_r\theta} d\theta \right\rangle . \tag{2.20}$$

The rotation is only present when the magnet is powered (at the correct frequency), so that an arbitrary axis in the plane of rotation can be set by adjusting the time the magnet is in action. Figure 2.5 shows such a behaviour as measured in COSY during the 2012 JEDI beamtime.

2.2.4 Froissart-Stora-frequency scans

In 1959 Froissart and Stora (FS) first theoretically described the spin evolution close to a spin resonance [15]. In the theoretical case where the frequency of a spin-manipulating B-field is swept from zero over a single spin-resonance with the constant speed $\alpha = \Delta f/\Delta t$ the polarisation after the sweep P_f in respect to the polarisation before the sweep P_i is given by the FS-formula where f_c is the cyclotron frequency and ϵ is the resonance strength [15, 16, 11]:

$$\frac{P_f}{P_i} = 2 \cdot \exp\left[\frac{-(\pi\epsilon_{FS} f_c)^2}{\Delta f/\Delta t}\right] - 1. \tag{2.21}$$

If the crossing speed α is small in respect to the resonance strength ϵ^2 the polarisation will be reversed. In the contrary case the spin is left almost unaffected. Anything in

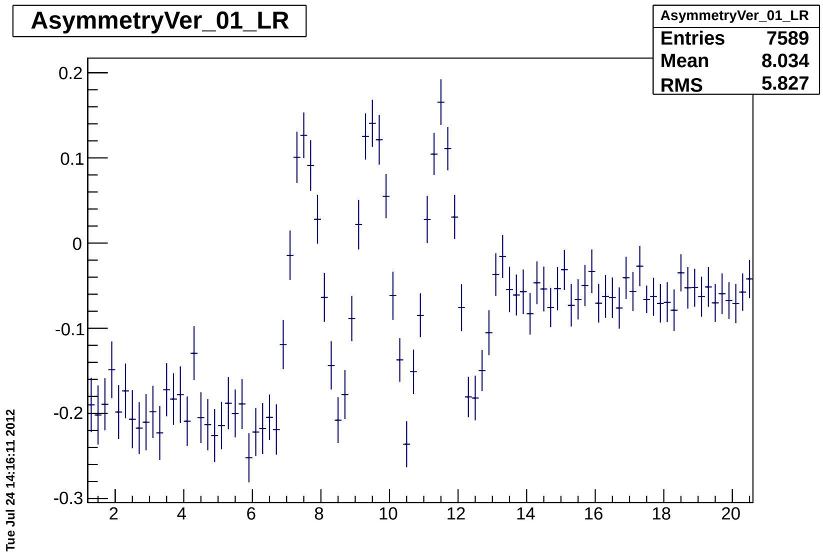

Figure 2.5: Spin oscillation with a RF solenoid

between will mean a partial loss of polarisation. The FS method can be used to cross resonance while preserving the polarisation or to measure the effective integral field of a magnet.

The orbit integral in 2.20 can be substituted with a line integral along the orbit ($d\theta = dl/r$) and the effective field can be expressed by the synchrotron condition ($e/p = 1/Br$). The resonance strength of the dipole magnet is then given by

$$\epsilon_{BDL} == \frac{1}{4\pi} \cdot \frac{e(1+\gamma G)}{p} \int Bdl = \frac{1}{\sqrt{8}\pi} \cdot \frac{e(1+\gamma G)}{p} \int B_{RMS} dl. \tag{2.22}$$

In an ideal accelerator, with only the RF spin-flipper, the resonance strength as calculated from the integral field of the flipper ϵ_{BDL} would be the same as one measures with a FS-scan (ϵ_{FS}). This can obviously not be true when the magnet is operated close to an (intrinsic) resonance as given by the rest of the lattice. The ratio $\epsilon_{FS}/\epsilon_{BDL}$ is well described by

$$\frac{\epsilon_{FS}}{\epsilon_{BDL}} = 1 + \frac{k}{|\nu_y - \nu_{RF}|}. \tag{2.23}$$

This expression diverges when the frequency of the RF magnet matches the vertical tune. k is a constant given by the lattice. For deuterons the situation is somewhat different as the whole frequency range is effected by overlapping higher order spin resonances. Previous measurements (SPIN@COSY 07/08) have shown an $\epsilon_{FS}/\epsilon_{BDL}$ of 0.15 ± 0.01 for deuterons at COSY far away from an intrinsic resonance [16].

2.3 Experimental method for EDM measurements

The basic idea of detecting EDMs at storage rings is based on the fact that spin and EDM always point along the same axis. So if one can build up a spin-rotation due to a none vanishing EDM (see BMT-equation 2.17), the resulting spin-angle can then be measured in a polarimeter.

2.3.1 Dedicated machine

Frozen-spin-method (FSM) [12]:

In order to maximize the EDM effect we wish to maximize the length of the exciting element. This can be achieved in an accelerator with electric bending and horizontal beam polarisation. The radial electric bending field then also tilts the EDM out of the horizontal plane. In order for this to work the spin must be always aligned with the momentum vector ($\nu_s = 0$). The BMT equation 2.17 can be rewritten in the case of a pure dipole accelerator in the momentum rest-frame neglecting the EDM to be

$$\Omega = \frac{e}{m}\left[G\vec{B} + \left(\frac{1}{\gamma^2 - 1} - G\right)\frac{\vec{\beta}\times\vec{E}}{c}\right]. \qquad (2.24)$$

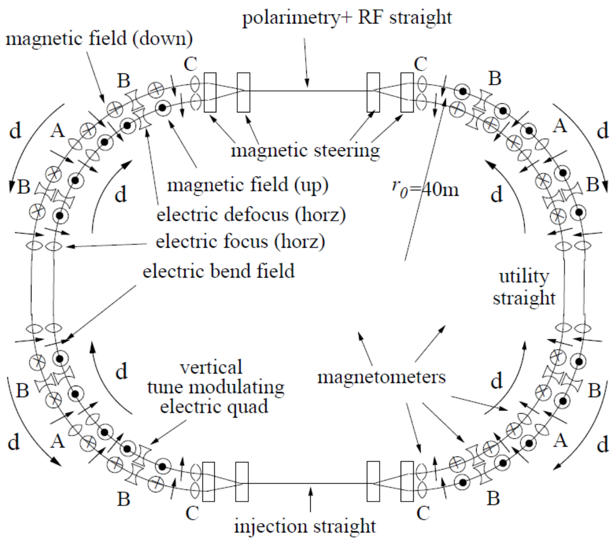

Figure 2.6: “All-In-One” ring for EDM measurements of p,d and ^{3}He [17]

In order to meet the above condition (ν_s) Ω is required to be zero. For the proton ($G \approx 1.8$) an all electric bending machine can be realised at around 0.7 GeV. For deuteron and ^{3}He a purely electric machine is not possible, due to the negative G factor. Richard Talman recently presented the basic layout of an accelerator that would be able to produce the fields needed to fulfill the FSM condition for all three types of particles (see figure 2.6) [17]. With some modifications to the design, this machine might even fit into the currently existing COSY building [18].

Spin-coherence-time (SCT)

In previous experiments, with the spins aligned vertically, spin coherence, this is their relative phase, has never been considered, as it did not effect the polarisation (see figure 2.7). This will be different in an EDM experiment as a loss of coherence will mean a loss of the horizontal polarisation (see again figure 2.7) and will thus stop the further buildup of EDM signal. The SCT in respect to an arbitrary axis $\vec{a}$ is defined by [12]

$$\frac{1}{\tau_{SCT}} = \left| \frac{1}{N} \sum_{j=1}^{N} \frac{1}{\vec{s}_j \cdot \vec{a}} \cdot \frac{d(\vec{s}_j \cdot \vec{a})}{dt} \right|. \tag{2.25}$$

The spin decoherence mainly arises from a momentum difference between individual particles and so a difference in spin tune. In an unbunched machine this effect is enormous as the spread in revolution frequencies is large between particles. In the case of a bunched beam the cavity forces the particles back into the center of the bunch, which results in a longitudinal oscillation (synchrotron oscillation) and an according oscillation of individual spins around the reference spin (windshield wiper motion). In this case an average momentum spread can only arise through different pathlength for particles with different betatron oscillation amplitudes [19].

The spin coherence time currently accessible at any hadron machine is in the order of dozens of seconds, with substantial effort on the way to increase this for example by utilising sextupole fields to flatten the pathlength distribution [19].

In the final experiment the tilt angle per revolution due to the EDM effect will (at an EDM of 10^{-24} $e$cm) be in the order of 10^{-12} rad. Which means that it takes around 10^{11} revolutions or 10^5 seconds until a measurable polarisation has been achieved. The SCT will have to be in the same order of magnitude .

Sensitivity

The statistical sensitivity of such an experiment, neglecting any systematic errors, is given by [12]

$$\sigma \approx \frac{3\hbar}{P \cdot A \cdot E_R \cdot \sqrt{(N_{Beam} f_c T_{total} \tau_{spin})}}. \tag{2.26}$$

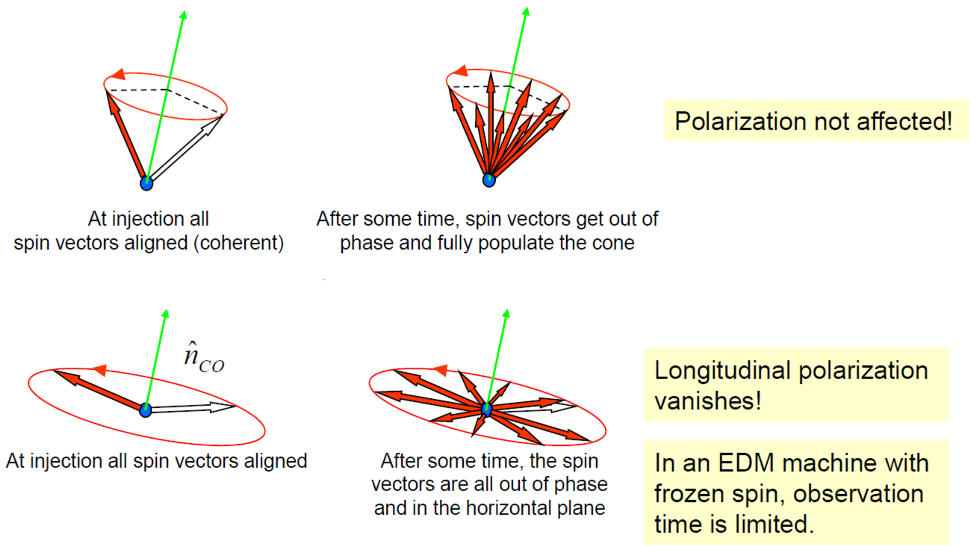

Figure 2.7: Spin coherence [12]

A and f are the polarimeter analysing power and efficiency respectively. P and N_{beam} describe the beam polarisation and total number of stored particles. E_R denotes the radial electric field that tilts the EDM. T_{tot} and τ_{spin} are the total running time per year and the spin-coherence-time (see section 2.7).

Assuming a number of feasible values a sensitivity of around $3 \cdot 10^{-29}$ $e$cm seems possible [1].

2.3.2 Systematics

Whenever trying to set limits on a minutely small quantity, systematics that mimic the same behaviour as the searched for quantity have to be carefully considered. Going back to the BMT equation 2.17 we see that in a machine with radial (horizontal) electric holding fields, non average vertical electric and horizontal magnetic fields would also result in a vertical tipping of the spin, as expected for the EDM.

A rough estimation from the current deuteron EDM limit already calls for a ratio of average vertical electic field to the horizontal field of below 10^{-10}. Precision at this level will need a substancial design, placement and commissioning effort. During the runs even the room temperature will eventually have to be controlled [12].

This is only the leading systematic effect. Other effects for example involve the windshield wiper motion, which will call for a fast polarimeter to monitor the frequency stability and frequency locking of the RF magnet and the cavity. The actual measurement will most likely not be dominated by the sensitivity discussed in section 2.3.1, but by the systematic errors.

2.3.3 Preliminary experiments at COSY

Before being able to build a dedicated machine, about a decade from now, a number of issues have to be studied in further depth. Among these are SCT, polarimetry, RF-E fields with high field strength, systematic effect of unwanted field components and spin dynamics simulations.

To study systematics it is unreasonable to try and manipulate the unknown EDM. Fortunately the effect of EM-fields is principally the same on the EDM as it is on the MDM (see BMT-equation). Therefore all systematics can be studied by manipulating the well-known MDM. The RF magnet that will be presented and investigated in this theses is supposed be be used for investigations concerning the effect of different RF waveform shapes on the SCT and to learn to deal with unwanted field components.

Once these issues have been looked at seperately the JEDI collaboration then aims to conduct a first direct EDM measurement with a sensitivity of around $d = 10^{-24}$ $e$cm [1]. For this a short section of RF-E field will be utilised, that tilts the initially vertical spin into the accelerator plane.

2.4 COSY

The COoler-SYnchrotron (COSY, see figure 2.8) at the Forschungszentrum Jülich can provide vertically polarized H^- and D^- beams with energies from 300 MeV (H^-) / 600 MeV (D^-) to 3.7 GeV for internal as well as external targets.

The ring has a circumfrence of 183.4 m which includes two straight sections for experiments and diagnostics. The emittance of stored beams at injection energy is reduced by injecting a highly ordered electron beam into a small section of the accelerator (electron cooling). Above $\beta = 0.85$ stochastic cooling can be utilised for the same purpose. It consists of a set of pick-up electrodes that sense the particle distribution in respect to the orbit within one bunch. Their signal is transported to a set of kicker electrodes with the proper phase, where it is used to correct the particle position and effectively reduce entropy [11, 13].

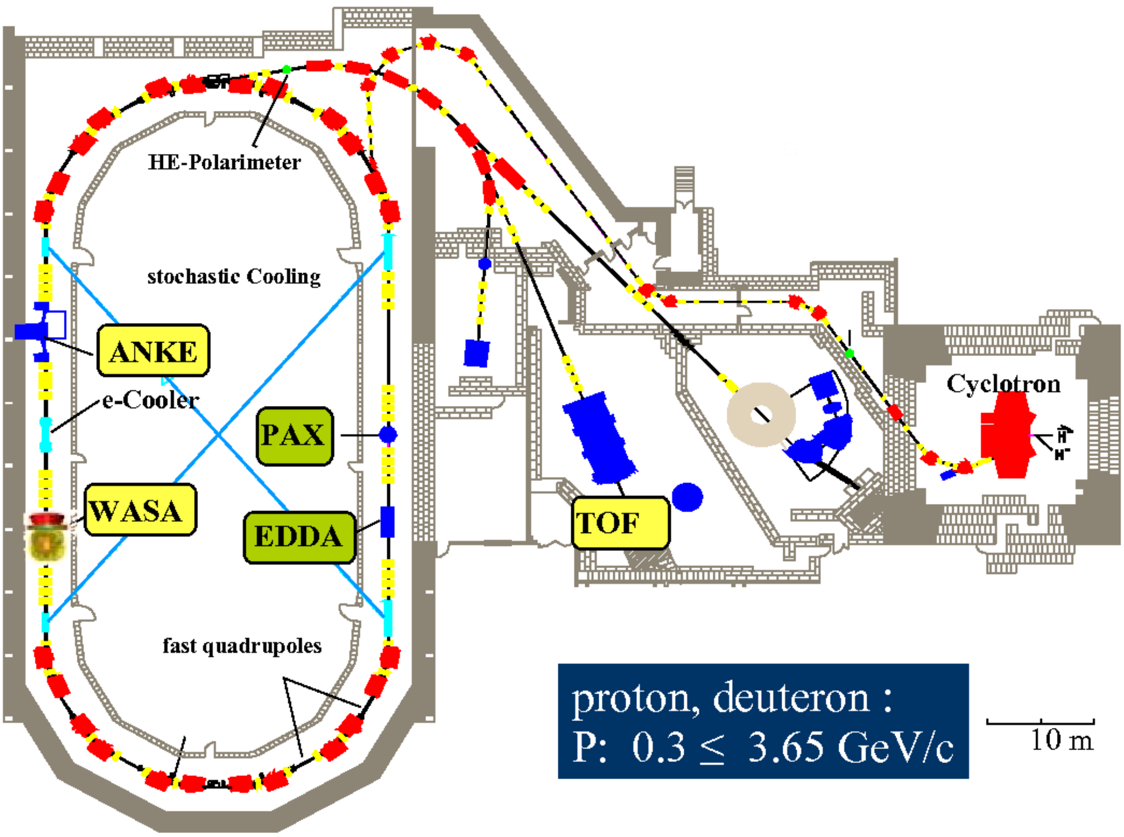

Figure 2.8: COSY accelerator facilities [20]

2.4.1 EDDA-polarimeter

Figure 2.9 shows a schematic of the EDDA polarimeter, the internal COSY experiment that is used to determine the beam polarisation. It consists of two layers of interwoven scintillators and covers the forward region of a solid scattering target [13]. During the 2012 beamtime this was a hollow carbon rectangle. The vertical polarisation of the beam is directly linked to the count-rates left and right (horizontally) from the target, by the energy dependent analysing power.

$$\epsilon = P_y \cdot A_y = \frac{N_R - N_L}{N_R + N_L} \tag{2.27}$$

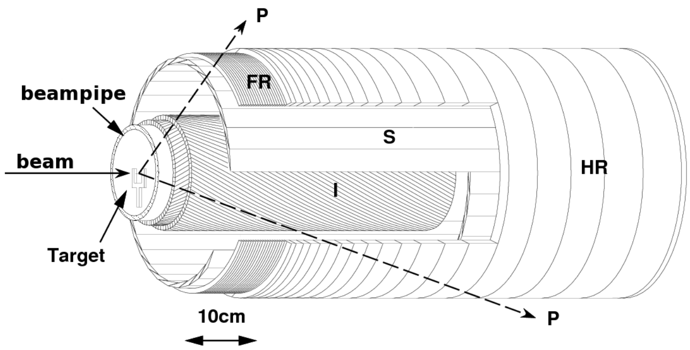

Figure 2.9: Schematic of the EDDA polarimeter [13]

3 Magnet design

The JEDI proposal states the following requirements for the new RF-B flipper:
"A broad-band RF-B spin flipper has to be utilized to have the capability to apply magnetic fields with different wave forms and over a wide frequency range (roughly 80 kHz and 1 MHz). The required integral field strength depends on the momentum spread of beam and will roughly be 0.025 Tmm. The intended system is able to deliver a RF-B field over a wide frequency range and is based on a stripline design (transverse electromagnetic (TEM) transmission line)." [1] The expected frequency range was later extended to 1.5 MHz. Higher frequencies generally allow a more precise shaping of the desired waveform. The integral field of 0.025 Tmm has to be understood as field amplitude and not as effective field.

3.1 Geometry

In order the meet the design criteria the following design has been proposed and realised [21]:

The magnet is made up of four independent stripline units, each being build from 1 mm copper plates, which are arranged as shown in figure 3.1. The outer conductor is 65 cm long and 5 cm wide. The inner conductor is slightly smaller at 61 cm $\cdot$ 3.5 cm and separated from the outer conductor by a 1 cm gap. This geometry guarantees an impedance (see next section) of 50 Ω for each stripline unit, which is needed for a lossless coupling of the magnet to an amplifier via coaxial cables. This value has been confirmed by Ralf Gebel and can be reproduced in simulation (see chapter 6).

Opposing stripline pairs are separated by 8 cm to allow for a good fit around a rectangular ceramic chamber, which functions as beam-pipe at the position of the magnet in COSY. Neighbouring striplines can either be directly adjacent (compact geometry) or can be separated by a 5 cm gap (extended geometry).

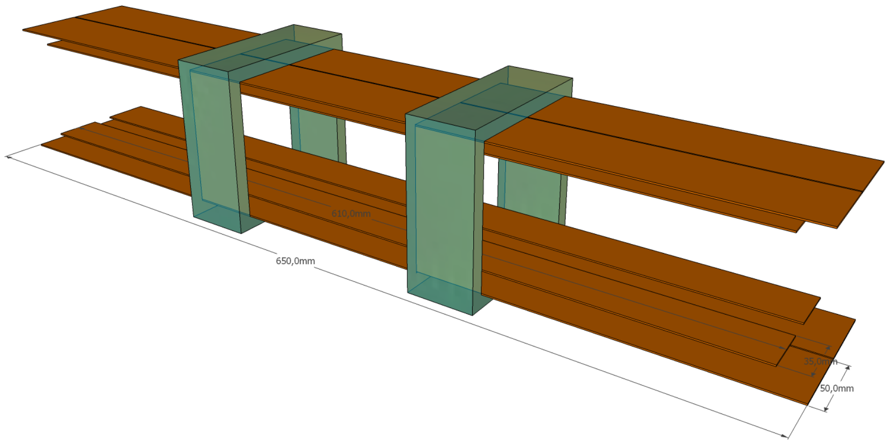

Figure 3.1: CAD view of the stripline magnet in compact geometry

3.2 Transmission line theory

All aspects of electromagnetic fields and circuits can be derived from Maxwell's equations (here given in differential form):

$$\nabla \cdot \mathbf{E} = \frac{\rho}{\epsilon_0}, \tag{3.1}$$

$$\nabla \cdot \mathbf{B} = 0, \tag{3.2}$$

$$\nabla \times \mathbf{E} = -\frac{\partial \mathbf{B}}{\partial t}, \tag{3.3}$$

$$\nabla \times \mathbf{B} = \mu_0 \mathbf{J} + \mu_0 \epsilon_0 \frac{\partial \mathbf{E}}{\partial t}. \tag{3.4}$$

The magnet is operated at a frequency of about 1 MHz. This frequency is equivalent to a wavelength of 300 m. Even with all conductors wired in series the total length of the magnet is orders of magnitude shorter. This in turn means that for any given point in time the phase of the current is nearly constant all over the magnet. It should thus be a rather good approximation to calculate the circuit properties based on standard circuit theory (lumped element method) and to neglect all dynamics when calculating fields.

In the lumped element method a transmission line such as the stripline elements of the magnet can be thought of as an infinite series of elements as shown to the right. In order to calculate characteristics the elements can be added to one effective schematic and the overall impedance can be derived from this as follows:

The general solution containing incoming (I_+) as well as reflected (I_-) currents is given by

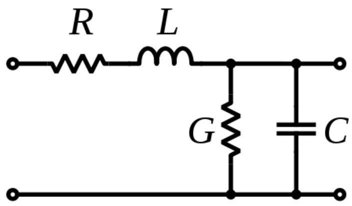

Figure 3.2: Transmission line schematics ($R, G \approx 0$)

$$U(x,t) = \hat{U}_+ \exp(i\omega t)\exp(\gamma z) + \hat{U}_- \exp(i\omega t)\exp(-\gamma z). \tag{3.5}$$

Applying Kirchhoff's circuit laws

$$\gamma \hat{U}_+ = R\hat{I}_+ + i\omega L \hat{I}_+, \tag{3.6}$$
$$\gamma \hat{I}_+ = G\hat{U}_+ + i\omega C \hat{U}_+, \tag{3.7}$$

yields the characteristic impedance

$$Z_0 = \frac{U_+}{I_+} = \sqrt{\frac{R + i\omega L}{G + i\omega C}} \approx \sqrt{\frac{L}{C}}. \tag{3.8}$$

The actual impedance of a device is only equivalent to the characteristic impedance if no reflections occur. This is true for an infinite transmission line or (and practically actually relevant) if the device is terminated by its characteristic impedance [22, p63].

In a laboratory environment the standard waveguide is a 50 Ω coaxial cable. The impedance of the stripline and of the terminating resistor have to match this value to avoid partial reflections at transition points. For a simple stripline made of two infinite plates of width w, spaced d apart the impedance is given by

$$Z_0 \approx \sqrt{\frac{L}{C}} = \sqrt{\frac{\mu}{\epsilon}\left(\frac{d}{w}\right)^2} = 377\Omega \frac{d}{w}. \tag{3.9}$$

3.3 Wiring scenarios

The great number of conductors allows for a variety of wiring schemes. One has to distinguish between two different operation modes:

1. Stripline mode: Currents flow through the outer conductors as well as the inner conductors. The current on the outer conductor is opposite to the current on the inner conductor.
2. Classical mode: Currents only flow through the inner conductors. The 50 Ω impedance is lost in this mode when the magnet is operated at high frequencies. Whether losses due to reflections are negligible has to be further investigated. In the following the device is always assumed lossless.

For the sake of a simple and accurate terminology lets define the following coordinate system: The origin sits at the center of the magnet, which will be the region the beam passes through. The X-axis points along the direction of beam, this is along the long side of the magnet. The Z-axis points along the short side of the stipline plates and the Y-axis point into the plane of conductors.

From now on only the direction of current on the inner conductor will be denoted, this is done by crosses and arrows (see figure 3.3) in the same fashion as one is used to from field vectors.

The main component we are interested in is B_z. In order to achieve a strong field in this direction wiring 1 has to be used. Rotating this configuration by 90 degrees yields wiring 3, which gives a strong B_y component, which can be used for systematic studies of unwanted field components. The extended geometry is optimised to produce equally strong fields into the z and y direction, depending on the wiring.

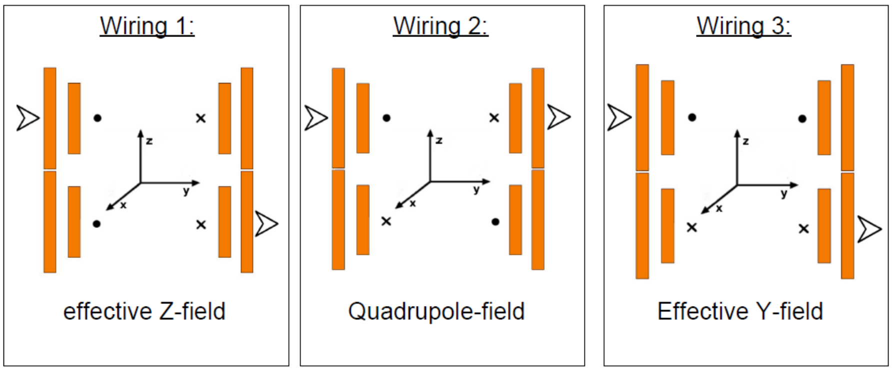

Figure 3.3: Different wiring schemes

Another sensible wiring scheme, in which currents through neighbouring units are always opposite is denotes as wiring 2. The expected field has a quadrupole arrangement and is thus of minor interest.

4 DC analytical model

In order to be able to quickly produce good field estimates, an analytical model is supposed to be established. As we have already seen, it is a good approximation to neglect all dynamics in Maxwell's equations. The fields can thus be deduced from the charge and current densities alone.

For the complex geometry of the magnet this is analytically still rather challenging. As a further simplification we may substitute the copper conductors for one-dimensional current densities and consider these to be infinite in length. The magnetic field of an infinite pointlike wire at origin is given by:

$$\vec{B}(\vec{r}) = -\frac{\mu \vec{I}}{2\pi} \times \frac{\vec{r}}{r^2}. \tag{4.1}$$

The field of the magnet can be deduced from this equation by integrating over the current densities. The z component of the magnetic field somewhere on the z-axis is then for example given by:

$$B_z(z) = -\frac{\mu}{2 \cdot \pi} \sum_{conductor_i} \int_i \frac{I}{l_i} \cdot \frac{y_i}{y_i^2 + (z - z')^2} dz'. \tag{4.2}$$

l_i and y_i denote the length and central y value of conductor i. The following section shows the resulting field strength of wiring 1 in both operating modes and geometries. This is supposed to give a first impression of the magnets field and is to be used for later comparison against measurements and simulations.

4.1 Classical mode - wiring 1

Figure 4.1 shows the B_z component along the z-axis for the classical mode in wiring 1 and has been generated with a current of 1 A on each conductor. The field strength in compact geometry is nearly constant in the region of interest around the origin at around 0.145 G/A.

Assuming an effective length of 60 cm would require a peak current of 2.9 A, which is equivalent to a power of 200 W at the usual RF impedance of 50 Ω. At the time of first commissioning this was exactly the power that was available from the amplifier.

In the extended geometry the B_z field strength at the point of beam passage is reduced by approximately 50% compared to the compact geometry. For the B_y component on the y-axis a similar result to equation 4.2 can be found for wiring 3:

$$B_y(y) = -\frac{\mu}{2 \cdot \pi} \sum_{conductor_i} \int_i \frac{I}{l_i} \cdot \frac{z_i}{y^2 + (z')^2} dz'. \tag{4.3}$$

At the origin this yields a B_y of 0.1, which is approximately the same as the B_z strength in wiring 1. We can thus conclude that the ability to produce equally strong fields in y and z should be met in classical mode.

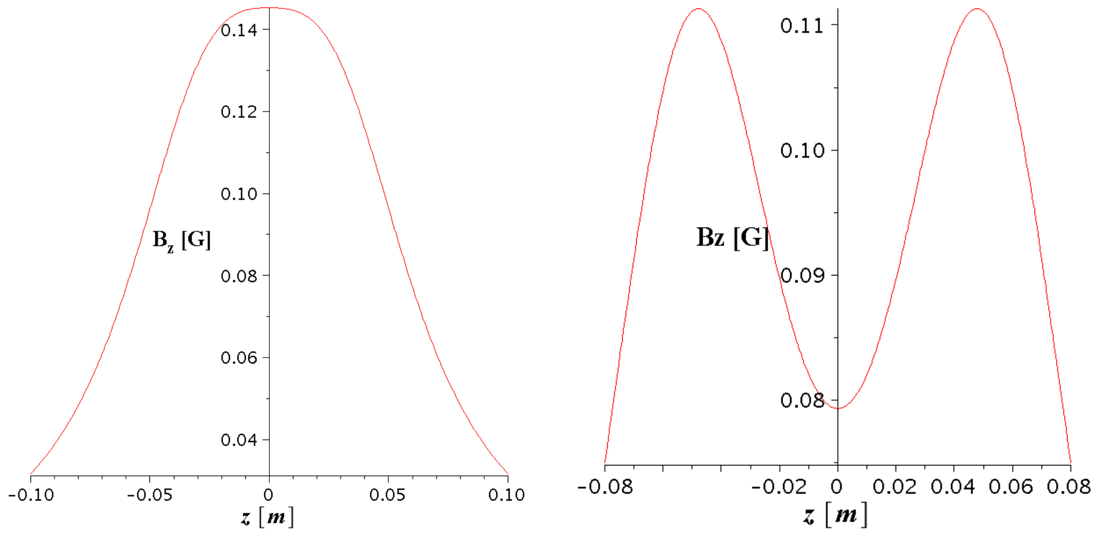

(a) Compact geometry

(b) Extended geometry

Figure 4.1: Classical mode - wiring 1

4.2 Stripline mode - wiring 1

Figure 4.2 shows the $B_z(z)$ behaviour in stipline mode, generated at a current of 21 mA. This has been chosen as the later alternating field measurements were conducted at a mean current of 15 mA. The central field in compact geometry is severely reduced in comparison to the classical mode, due to the outer conductors contributing an opposing field. At 21 mA the central field is $42 \cdot 10^{-5}$ G small, which is 0.028 G/A and factor 7.25 smaller than in classical mode. Accordingly a 11 kW amplifier would be needed to reach the required field.

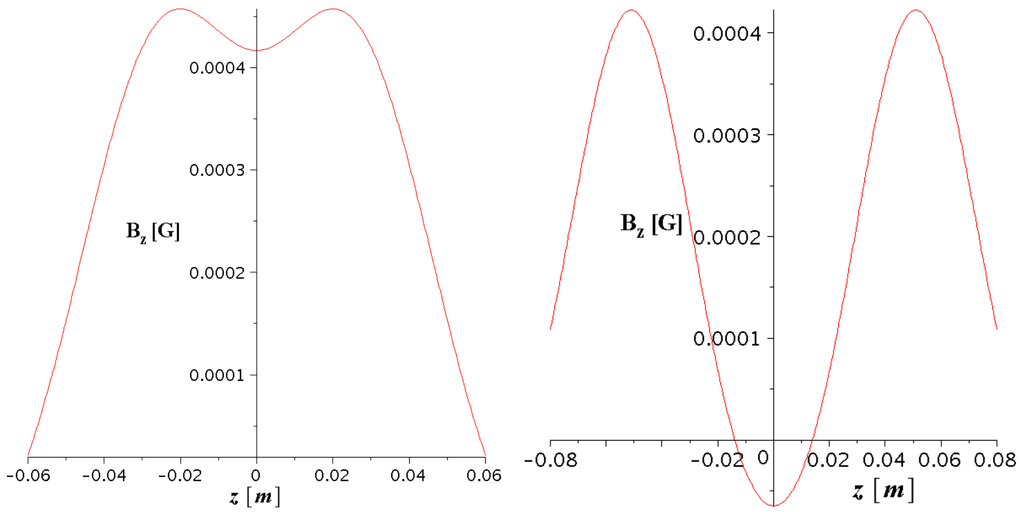

(a) Compact geometry

(b) Extended geometry

Figure 4.2: Stripline mode - wiring 1

For the extended geometry the situation is even worse, as the central field is tiny at less than a quarter of the field in compact arrangement and is furthermore negated in respect to the rest of the central magnet.

In order to understand this behaviour the central B_z strength is plotted vs. the separation of neighbouring conductors in Figure 4.3a shows such a plot. For the sake of simplicity the conductors have been substituted by point currents. The y-axis has not been scaled to give any meaningful fieldstrength and is only supposed to show the sign. It is found that the central field quickly vanishes with growing separation, the field negation then takes place at around 9 cm. In the extended geometry the central point of the neighbouring conductors are 10 cm apart. Although finite element field simulations are only introduced later (see section 6) figure 4.3b indicates that the 'return fields' within the stripline units spread into the center of the magnet as the separation increases.

Should this behaviour be confirmed in later measurements, we can then rule out the extended geometry in stripline mode for any useful purpose.

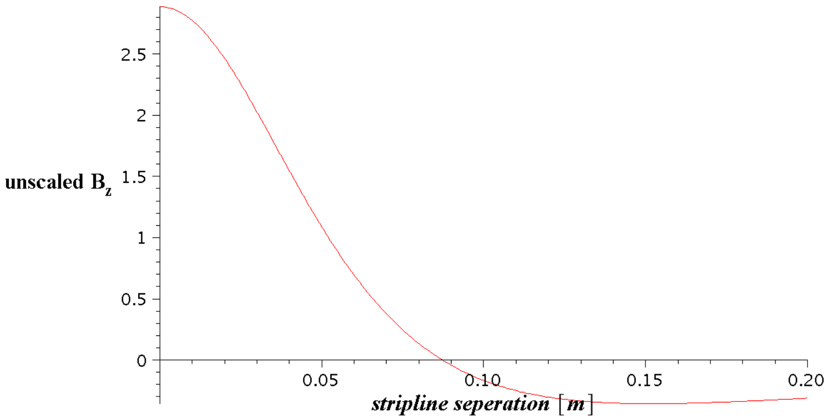

(a) B_z negation as a function of separation

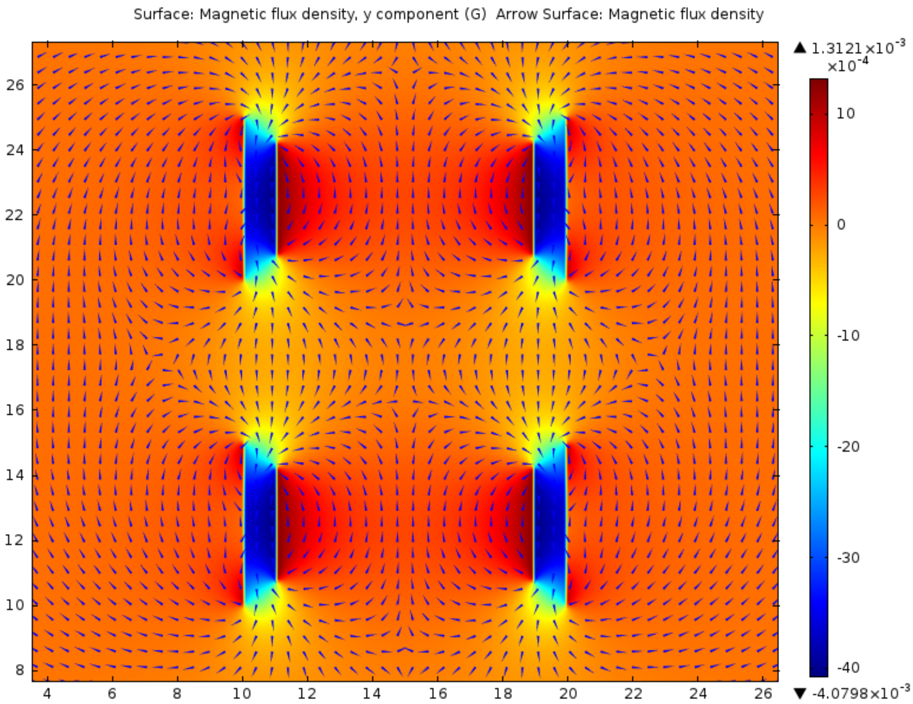

(b) COMSOL simulation for a seperation of the outer conductors of 5 cm

Figure 4.3: Field negation in extended geometry

5 Field measurements

In order to evaluate the field strength and field geometry under a great variety of circumstances a number of measurements have been carried out. In order to establish field strength and homogenity in classical mode a spacial scan of the magnet powered by DC (static field) has been performed. In a second set of measurements the stripline and frequency characteristics have been studied.

5.1 Static field

5.1.1 Experimental setup

3D Hall-magnetometer

For the DC measurement a three-axis Hall Magnetometer (THM1176) from Metrolab Instruments has been utilised. The Hall voltage is a charge separation inside a conductor, which arises from an equilibrium state between the magnetic force on the conduction electrons moving with an effective velocity and the electric force due to the produced charge separation. The actualprobe inside the THM1176 has a sensitive area of 5.3 mm · 1.3 mm and is encased in a 10 mm · 16 mm plastic housing [23].

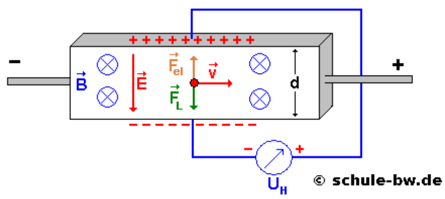

Figure 5.1: Sketch of the Hall effect

The manufacturer specifies a sensitive frequency bandwith from DC to 1kHz and a resolution of an offset corrected measurement of 1% of the selected operating range, which for our case is 0.03 G [23].

Prior to the actual field measurement some characteristics of the Hall probe were investigated. The Hall voltage is directly proportional to the current through the probe and is thus temperature dependent in the same way the resistance is temperature dependent. Figure 5.2 shows a scatter plot of the absolute magnetic field of 22000 data points sampled over 22 minutes in respect to the temperature as measured by the same probe. A small yet statistical significant dependency on the temperature can be seen (0.01 G/500 temperature steps).

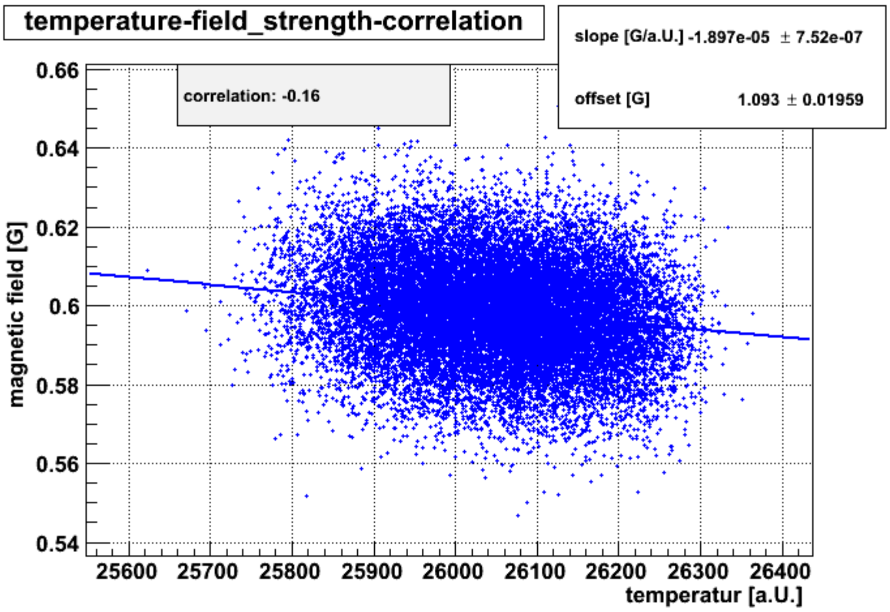

Figure 5.2: Temperature dependency of the Hall-magnetometer

From now on the temperature correction is always applied. Figure 5.3 shows the resulting field strength in respect to the time spent in the same measurement as above. The data is constant within the error of the slope. Projecting this graph onto the Y-axis (see figure 5.4) yields the statistical distribution of the measured B-field strength. The values exactly follow the naively expected Gaussian distribution. Each measurement has a statistical error of 0.012 (which is a factor 2.5 better than specified by the manufacturer (see page 5.1.1). The mean of around 0.6 G is the local strength of the earth magnetic field, which is an unwanted background to all following DC measurements.

Measuring procedure

In order to evaluate the field geometry a X-Y table with a 5 mm scale division has been built (see figure 5.5).

The field measurement is very sensitive on surrounding paramagnetic material. The field was for example already greatly disturbed when the magnet was fixed to the X-Y table with the help of a thin steel plate, which was in turn replaced by an aluminium plate. The magnet is therefore separated from the metal components of the X-Y table by a 2 cm PVC plate.

Due to the laboratory environment (lots of currents, magnets and paramagnetic materials) the strength of the environmental magnetic field is expected to change significantly when the probe is moved by only a couple of centimeters. As a result the probe has been

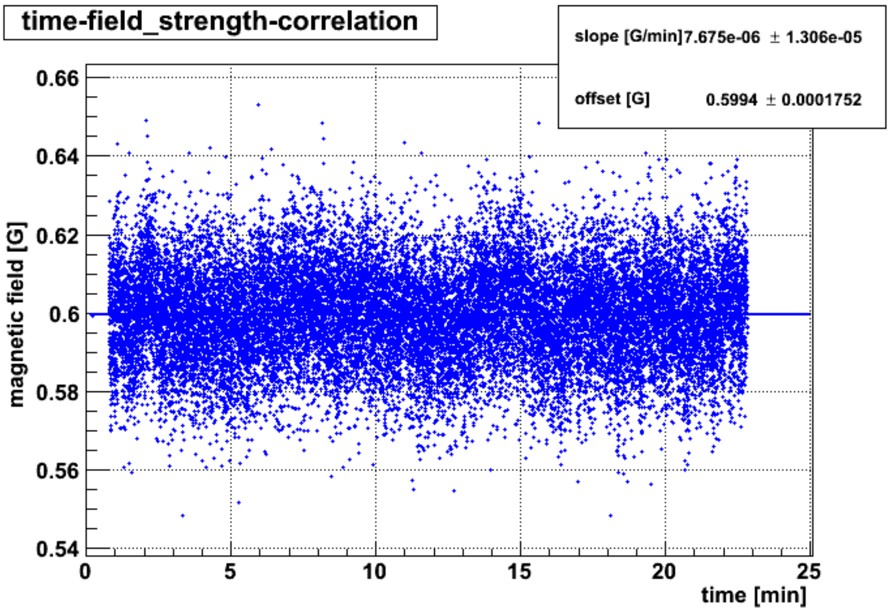

Figure 5.3: Time dependency of the Hall-magnetometer

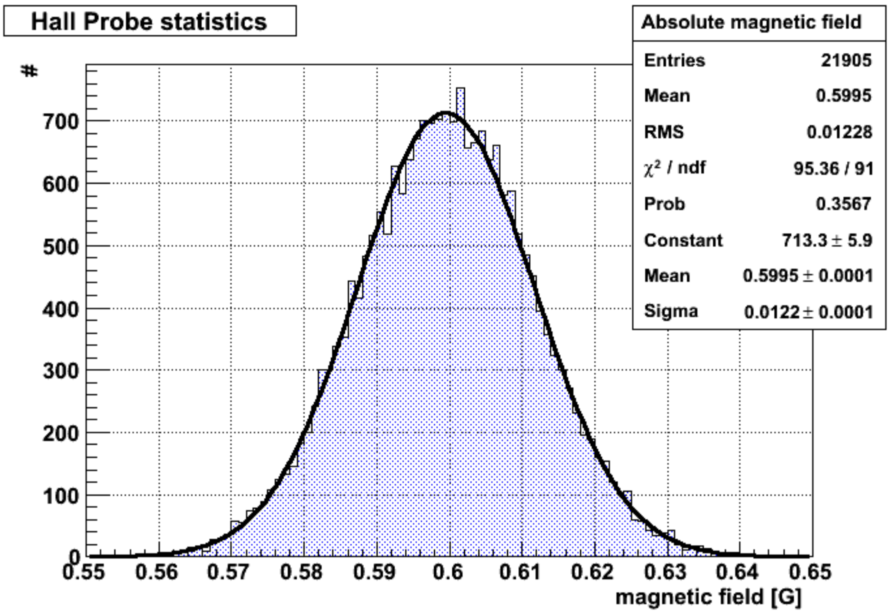

Figure 5.4: Statistical distribution of field strength values

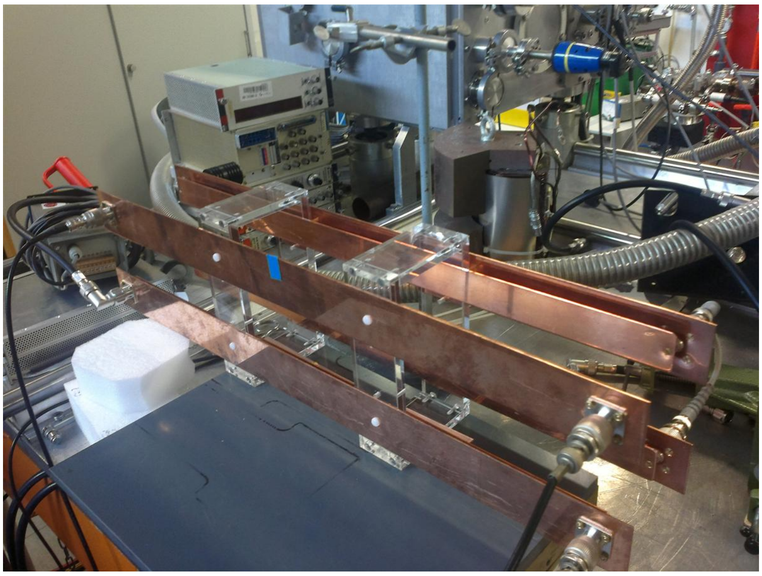

Figure 5.5: Stripline magnet with X-Y table and hall probe

placed statically and the magnet mounted on the X-Y table has been moved around the probe. There can still be minor changes to the field seen without currents on the conductors as the surrounding material changes as the magnet is moved. In order to cope with this problem background measurements have been carried out.

The whole of the magnet could not be scanned at once, due to obstructing plexiglas bars that keep the conductors in place and the fact that the movement of the X-Y table is limited to 20 cm in each degree of freedom. There were two sets of measurements performed:

Central region:
: The 15 cm $\cdot$ 8 cm central part of the magnet as defined by the plexiglas bars. The background field is expected to only change slightly within these bounds and has thus only been measured on the four edges. The spacial grid for measurement consists of $13 \cdot 7$ data point spaced 1 cm apart.

Fringe region:
: An overall 205 mm $\cdot$ 185 mm big region extending 80 mm further than the outer conductors. The background field has been scanned at 21 points spaced between two and three centimeters apart. The actual field measurement is made up of 63 data points (mostly) 2 cm apart.

In both cases the magnetic field probe was placed 38 mm below the upper edge of the magnet, which is almost central. The grid points were then passed in a sweeping motion, with a couple of hundred measurements being taken at each position.

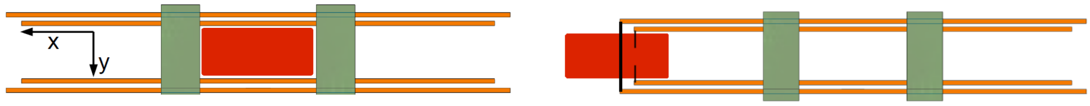

(a) central region (b) fringe region

Figure 5.6: Static field measurement regions

5.1.2 Results

The temperature correction has been applied around an arbitrary chosen value of 26000, before the values from each grid point have been averaged. By this procedure the fields with and without current on the conductors can be reconstructed. To obtain the actual field produced by the magnet the background field strength has to be substracted from the total field at each point. At points where no background measurement was available the strength of the background field was interpolated by the Delaunay algorithm. See figure 5.10 for an example.

The background and total fields are not absolute due to the arbitrary temperature correction offset. But as this offset is the same for both fields, the actual field generated by the magnet can be given without any temperature uncertainty.

In order to estimate the error on each field point two main contributions have to be considered:

1. The error on a single measurement has been established to be 0.012 G (see page 31). At each grid point around 300 data points have been taken. This makes for an error of 0.0007 G (0.07% at 1 G). The errors on the background values due to the Hall Probe are of similar magnitude, but cannot be considered purely statistical as each background point is being considered multiple times when calculating the field of the magnet alone.
2. The probe was only loosely fixed by a lab clamp, so that a perpendicular positioning is not guaranteed throughout the measurement. Assuming an angle error of four degree yields an error on each field component of 0.35% ($B_{real} = \cos(\text{angle error}) \cdot B_{measured}$). This error is also not purely statistical in between grip points due to the sweeping motion during field scans.

From the above two argumentations it is clear that no exact error on the field strength at any point on the grid can be given, although 0.4% seems like a very reasonable estimate. Typical values for the background and overall field are 0.2 G and 1 G. In the following we may thus consider each measurement field strength to have an error of 0.04 G.

Central region

Figure 5.7 gives the strength of the B_z component to be constant within errors within an area 4 cm wide. This as well as the field strength in this area (1.35 ± 0.04 G) is in accordance with the DC model extrapolated to 9A (1.31 G).

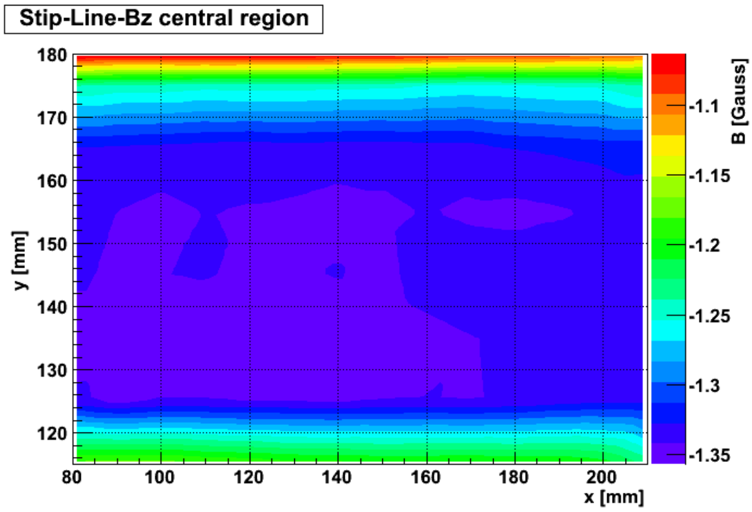

Figure 5.7: B_z central

The other field components B_x and B_y (figure 5.8) are consistent with zero in the region of interest.

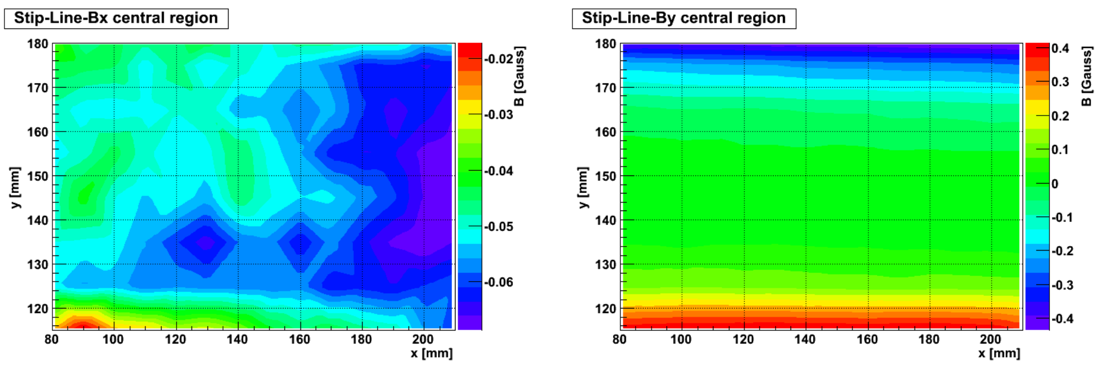

(a) B_x field

(b) B_y field

Figure 5.8: B_x and B_y in the central region

Fringe region

Figures 5.10 and 5.9 give the field strength distributions for all components of the magnetic field in the fringe region. The outer extends of the magnet are denoted by a solid line for the end of the outer conductors and a dashed line for the end of the inner conductors. Within the relevant region (about 1 cm around y = 150 mm) the unwanted field components B_x and B_y are consistent with zero (figure 5.9).

The B_z component can be seen to fall of smoothly (figure 5.10). From this behaviour one can also deduce an effective length (length of the field at maximum $B_z = 1.35$ G) of the magnet. The data points in figure 9.3 (appendix) have been taken from the y = 150 mm line. The statistical error is assumed to be twice the error of the probe on a single datapoint (0.0007 G), due to the slightly systematic nature of the errors on the background. The error due to an angle of the probe has not been considered as it should be purely systematic for a single sweep line. The fall off behaviour can be nicely approximated by a quadratic function. The resulting effective length (also considering the error on the maximum strength as statistical) comes out to be 565 ± 5 mm, which is around 85 mm short of the length of the inner conductors. From the effective length (565 ± 5 mm) and the central field (1.35 ± 0.04 G @ 9A) the integral field for wiring 1 in classical mode and compact geometry follows to be

$$\int B\mathrm{dl} = (0.00848 \pm 0.00026) \text{ Tmm/A} = (0.0240 \pm 0.0007) \text{ Tmm @ 200 W AC} \quad (5.1)$$

which is in a nice agreement with the DC analytical model.

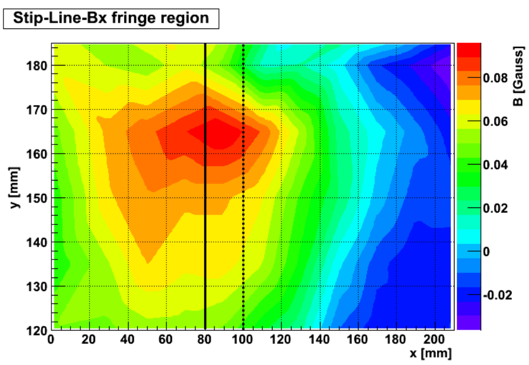

(a) B_x field

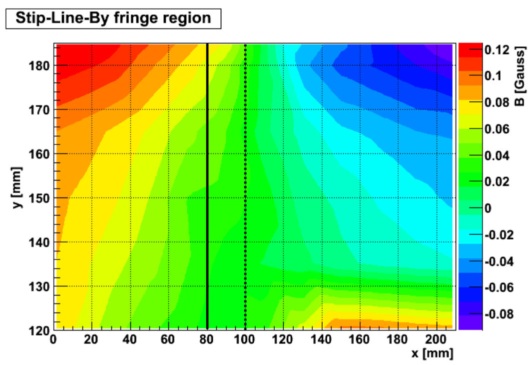

(b) B_y field

Figure 5.9: B_x and B_y in the fringe region

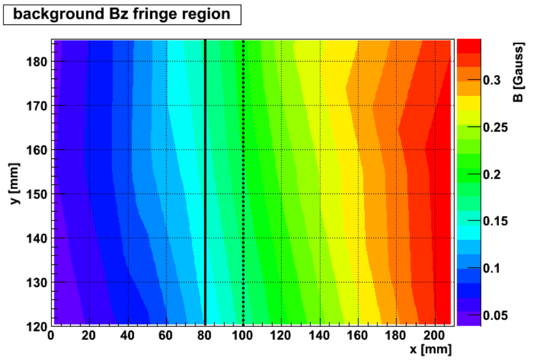

(a) Background field

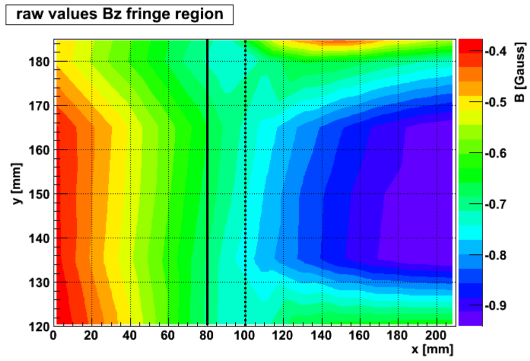

(b) Raw values

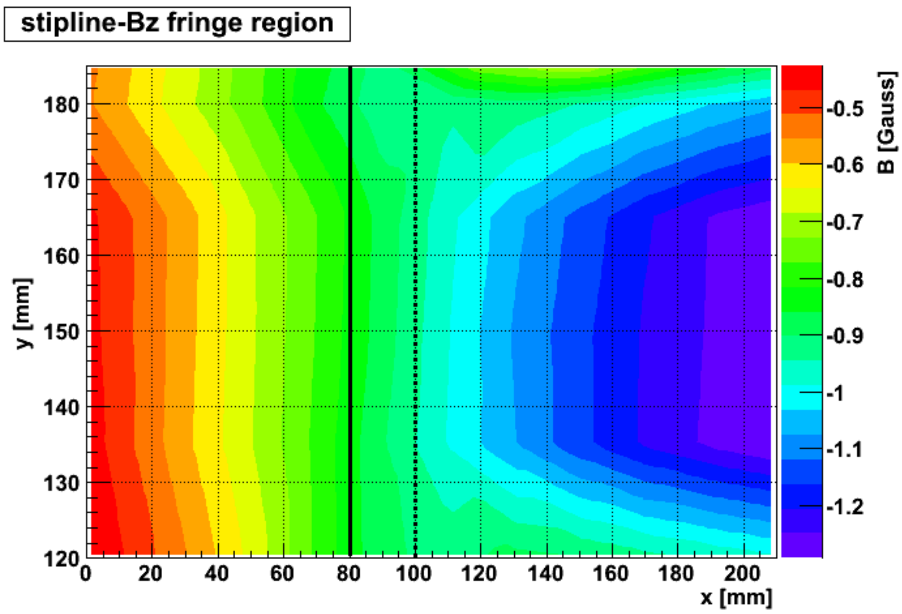

(c) Resulting field

Figure 5.10: B_z strength extraction from background and data fields

5.2 Alternating field

5.2.1 Experimental setup

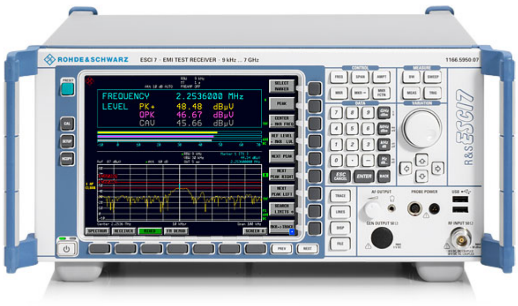

(a) R&S test receiver [24]

(b) E and B probes [25]

Figure 5.11: Equipment used for the AC measurements

Measurements of alternating fields at the design frequency range cannot be done with the previous discussed Hall probe. Precision measurements at these frequencies are generally tricky and involve costly and bulky equipment, usually only with the capability to measure absolute field strength and not single components.

Due to the limited time and resources available before the scheduled beamtime it was decided to use an R&S Test Receiver (ESU8 EMI) in combination with a set of magnetic and electric field probes (HZ-14), which were available from a neighbouring electronics institute. The set is commonly used for electro-magnetic-compliance tests, where troublespots have to be identified on a circuit-board, but is also advertised as field strength measurement equipment.

The magnetic field probe measures the field component parallel to the long edge of the probe, while the E probe only measures the absolute field. The internal mechanism of the probes is not presented by the manufacturer, but the antenna factor that converts the voltage output of a probe into an actual field strength (E or H field) is given in the manual. The antenna factor for the E field probe is given to be constant at 67 dB [25]. For the B probes see figure 5.12.

In the considered range between 0.1 MHz and 1.5 MHz this antenna factor can be parametrized by:

$$antenna = \left(70 - 17.14 \cdot f_{var} \cdot \ln\left(\frac{f}{1\text{MHz}}\right)\right) \text{dB}. \qquad (5.2)$$

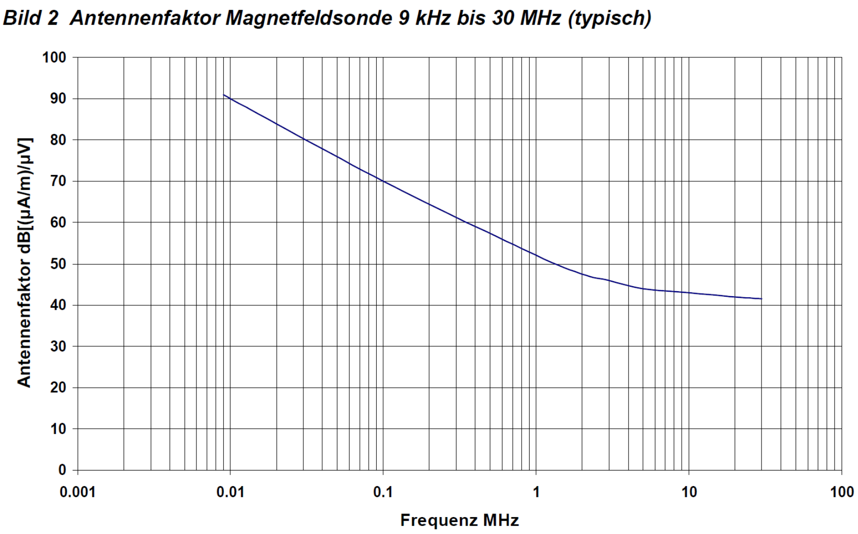

Figure 5.12: Antenna factor for B-field probe [25]

The factor f_{var} is introduced to later estimate the systematic effect of slight discrepancies of the antenna factor from the given graph. For a probe with the same behaviour as described in the manual f_{var} is equal to union.

During measurements with the B probe an additional preamplifier has been utilised. Its frequency dependent amplification curve (figure 5.13) has also been considered, but is almost constant compared to the antenna factor.

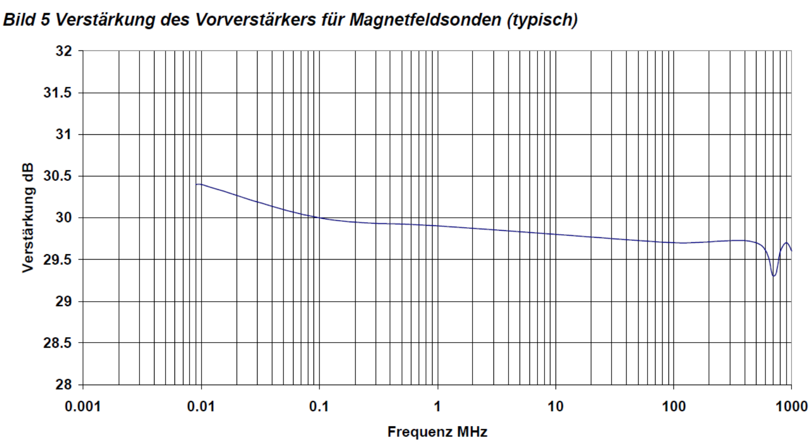

Figure 5.13: Amplification factor for the preamplifier [25]

The R&S spectrum analyser was operated in receiver mode. This means that only fields that oscillate at a frequency bandwith of 9 kHz around the set frequency are being measured [24]. The device was set to operate as quasi-peak detector, which weighs a signal by its repetition rate to give an annoyance factor. In our case of a continuous (sinusoidal) wave, this is luckily equivalent to a measurement of the peak value [26].

With this equipment the following two measurement procedures were repeated for both available geometries and all possible wirings (except wiring 2 expended geometry) in stripline mode at an effective current of 15 mA :

Frequency dependent central components:

For each accessible component (z,x for compact geometry and all three for the extended geometry) the B probe was visually placed at a central position. The frequency was then varied from 0.1 MHz to 1.5 MHz in 100 kHz steps. At each frequency step the probe voltage (in dBV) with and without RF was recorded. An additional frequency sweep like this was done with the E probe.

B_z along the z-axis at 1 MHz:

The frequency of the RF was set to 1 MHz. The B probe was fitted with a 0.5 cm scale ruler and placed within a styrofoam block, that could only be put at one well defined position in between the inner conductors. The probe was then retracted in 0.5 cm steps. At each step the voltage with and without RF was again recorded.

For each measurement the antenna factor (in dB) was added and the amplifier factor subtracted. The background and sum field strengths were then calculated from the dBV value:

$$B[T] = 10^{\frac{\text{signal [dB[V]]}+\text{antenna [dB[(A/m)/V]]}-\text{amplifier [dB]}}{20}} \cdot \mu_0, \tag{5.3}$$

$$E[V/m] = 10^{\frac{\text{signal [dB[V]]}+\text{antenna [dB[(V/m)/V]]}}{20}}. \tag{5.4}$$

The actual field produced by the magnet is again given by the difference between the sum and background field strengths. The statistical error on each measurement is given by 0.1 dB for background and 0.01 dB for sum field measurements. These values were in both cases chosen to be the last non fluctuating digit and have to be propagated to the final results.

5.2.2 Results

General remark

Figure 5.14a (blue curve) shows the frequency dependent B_z strength of a central point (compact, wiring 1, stripline mode), where the antenna factor has been chosen to exactly follow the description in the manual. At the 15 mA effective current the component is roughly $37 \cdot 10^{-5}$ G strong, which agrees roughly (10% diviation) with the DC analytical model (see page 28). In this graph, as in all the following, only statistical errors are drawn, which at least for magnetic measurements are negligibly small.

Over the whole frequency range all magnetic measurements show a quasi parabolic shape, where the maximum and minimum values are separated by almost a quarter of the maximum value. For red and green curve in figure 5.14a f_{var} (as defined in equation 5.2) has been varied to be 0.9 and 1.1. This slightly tilts the antenna factor straight and gives a maximum deviation of the antenna factor of 1.7 dB at 1.5 MHz. 1.7 dB is still significantly below the acceptable systematic deviation between probes of 3 dB specified by the manufacturer (3 dB is a deviation of roughly 50%), still the overall shape and the field strengths are severely different (i.e. nearely a factor two between $f_{var} = 0.9$ and $f_{var} = 1.1$ at 1.5 MHz).

Due to the strong dependency on the systematically hard to control antenna factor the measurements with the B probe can thus only be trusted in the resulting order of magnitude, which is of course not satisfactory for a field evaluation.

Figure 5.14 c shows the measured absolute E field (divided by c) over the frequency range for wiring 1. For the electric probe the antenna factor is constant, which reduces the systematical uncertainty. Over the whole frequency range the field is nearly constant at 11.4 V/m. The slight frequency dependence is exactly the same for all measurements, which hints to an internal characteristic of the probe. In an electro-magnetic wave the power is equally distributed within the electric and magnetic field. The absolute magnetic field is thus given by the electric field divided by the speed of light. In wirings 1 + 3 there is luckily always one component which is strongly dominant by one order of magnitude as seen with the B probe (i.e. compare figures 5.14 a and b). The strength of this component can thus be accurately measured (overestimated only by around 0.5%) from the absolute electric field.

When deducing the magnetic field strength from an electric field measurement an additional systematic has to be considered. All inner conductors were on a 0.75 V potential in respect to the common ground of the outer conductors and the test receiver. These potentials spread into the center and result in a non-zero electric field at points slightly off the central axis even when no currents are present. The strength of this parasitic field has been estimated from simulations (see section 6.2) to be 0.4 V/m ($0.9 \cdot 10^{-5}$ G) for each component at a point 3 mm off center.

The overall systematic error due to overestimation and the parasitic E-field is estimated to be 6%.

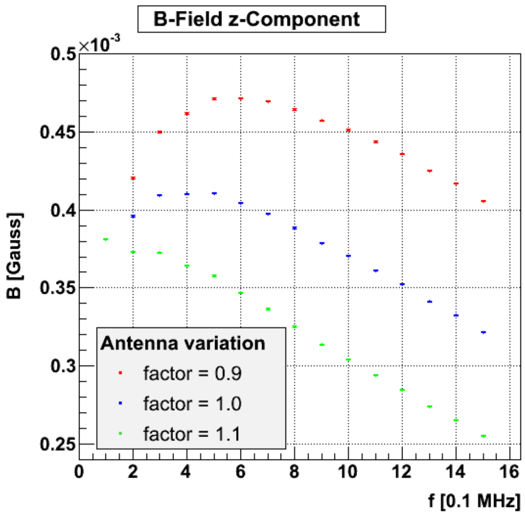

(a) B_z vs. frequency

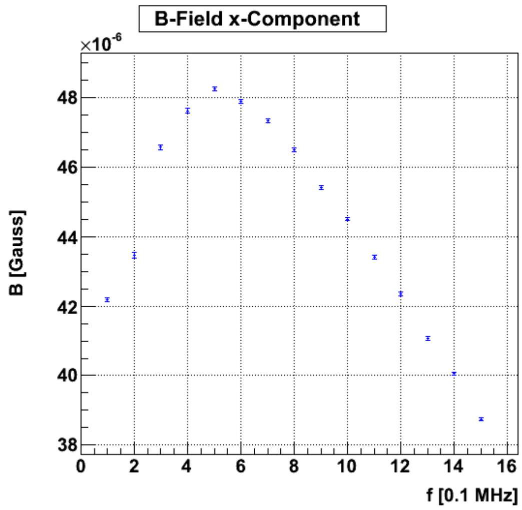

(b) B_x vs. frequency

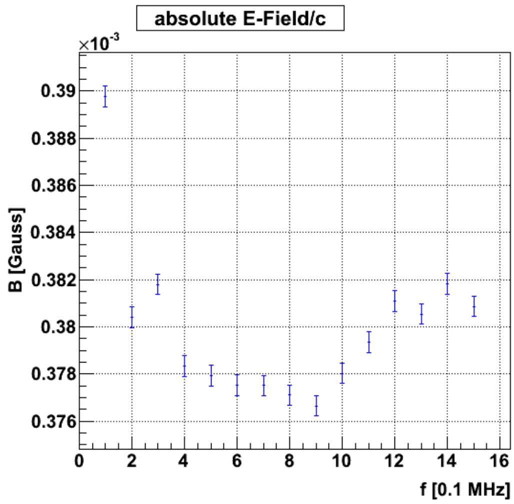

(c) $\frac{|\vec{E}|}{c} \approx |\vec{B}|$ vs. frequency

Figure 5.14: Compact 1 - Fields

Compact geometry - Wiring 1

Most aspects of this configuration have already been discussed above. Averaging over the magnetic field strength as measured by the E probe and only considering statistical errors yields a central B_z of $(38.0 \pm 0.3) \cdot 10^{-5}$ G @ 15 mA. Considering systematics yields: (0.0253 ± 0.0002) G/A.

The magnetic field probe can still be utilised to inspect the relative field changes along the z-axis. The according plot is given in figure 5.15a. The general behaviour is as expected from the DC analytical model. A more quantitative comparison can only be achieved when taking the 3cm y-extend of the sensitive volume of the probe into account. For this we need simulations (see page 48).

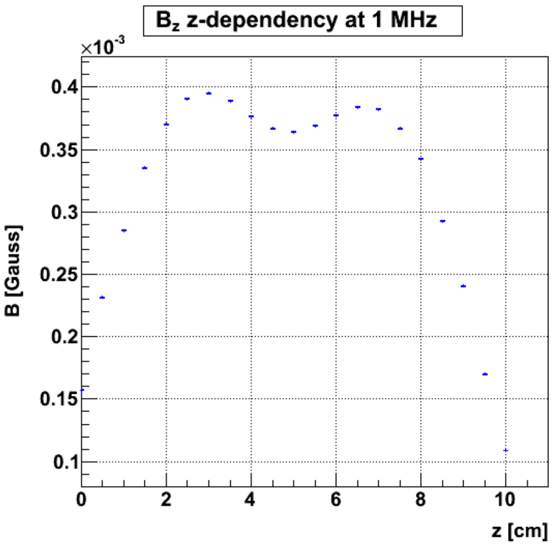

(a) Compact geometry

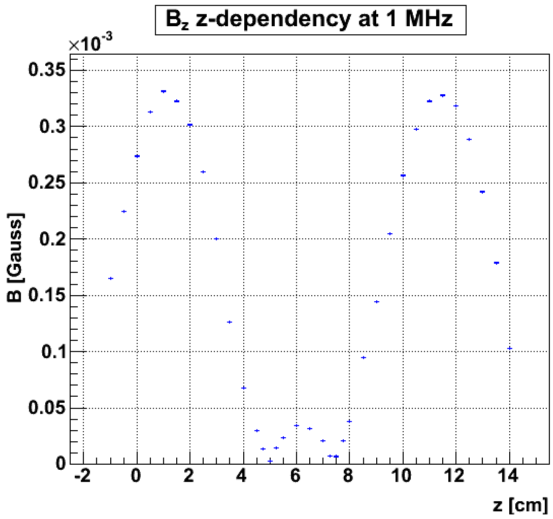

(b) Extended geometry

Figure 5.15: B_z along the z axis in wiring 1 both geometries

Compact geometry - Wiring 2

The whole set of measurements for this, as well as for all of the following setups, can be found in the appendix. The only thing worth mentioning for this setup is the B_z z-dependency, which nicely illustrates the quadrupole characteristic of wiring 2 (no field at the center, rising fields to the edges).

Compact geometry - Wiring 3

The dominant component is the y-component, which could not be measured in compact geometry due to obstructions. The other components are weak (around $15 \cdot 10^{-6}$ G) as expected. Due to this the B_z in z dependence measurement is quite noisy for both measurements in wiring 3. Within the styrofoam block the probe could slightly tilt which is believed to be the main problem when a non dominating component is measured in z-dependency.

Extended geometry - Wiring 1

From the DC analytical model it is suspected that this setup produces a negated and small field in the very center, which would basically render it useless for our purposes. Figure 5.15b shows the according measurement, which confirms this behaviour.

Compact geometry - Wiring 3

The B field probe shows that indeed component y is dominant. Comparing the electric field strength to the values measured for wiring 1 in extended geometry confirms that this geometry can indeed produce equivalently strong fields in the z and y direction.

For compact geometry wiring 2 (quadrupole arrangement) no measurement could be conducted before the magnet was installed in COSY. But, as we will see later, simulations can fill the gap (see page 45 onwards).

6 Simulation

Field measurements at the desired frequencies are limited by systematic uncertainties, so in order to cross check the measurements and to extend the dataset beyond the values accessible through measurements extensive simulations have been carried out. All considered toolkits rely on the finite element method, which basically discretizes time and space into a mesh and then numerically solves the differential equation of interest on the resulting grid.

A number of freeware packages (most prominently Poisson/Superfish by the Los Alamos Accelerator Code Group) are available. Poisson/Superfish is limited to 2D or axially symmetrical problems, while other programs only allow for a very limited mesh size. 2D simulations are sufficient to reproduce all of the measurements presented in the section on alternating field measurements, but in the end a reliable integral field has to be produced, which is only possible through 3D simulations.

Considering all these criteria it was decided to use the commercial COMSOL-Multiphysics software library. This toolkit enables simulations in a wide variety of areas. For our purposes only the AC/DC module is needed in addition to the basic installation. The whole program is controlled through a graphical user interface, where one starts out to define the geometry. This can be done to arbitrary precision (i.e. modelling coaxial cable feedthroughs), but every new detail introduces new systematics. In the presented simulation only the extends of the conductors were modelled. Next the corresponding material (copper for the conductors, air for the surrounding volume) and the desired current / voltage amplitudes are assigned to the geometric elements. The mesh is then generated automatically, considering the generally desired element size and taking into account different expected field gradients at different points of the model. Finally the fields are being simulated at the desired frequencies.

The size of the surrounding air area / volume is of major importance, as it's edges define the boundary conditions where the potential is set to zero. The simulated values will be wrong all over the mesh, if this does not match the actual physical situation. When first trying to reproduce the field of the extended geometry the total area was only 8 times as big as the magnet which resulted in a central field without field inversion. The total area was then increased to about 70 times the area of the magnet and the expected behaviour could be nicely reproduced.

2D and 3D simulations have to be done independently. As the computation time is strongly dominated by the size of the mesh, it is wise to first learn and refine the 2D simulations and only then convert the model to 3D. These spatial computations had to be done with a rather coarse mash and in DC approximation as any other settings resulted in computation timeouts or memory overflow.

In the following only results completing previous measurements are being presented.

6.1 Understanding the field inversion

In the DC analytical model and the alternating field measurements we have seen that at a very central point in the extended geometry wiring 1 the magnetic field is inverted in respect to the compact geometry. The same can be observed in the simulation (figure 6.1). Maxwells equations ($\nabla \cdot \mathbf{B} = 0$ as in section 3.4) demonstrate that magnetic field lines have to be closed. Following this line of argumentation the magnetic field within the stripline units can be thought of as the return field for the central field. As the neighbouring strip line units separate from the compact to the extended geometry, this return fields starts to spread into the central region until the central field is negated.

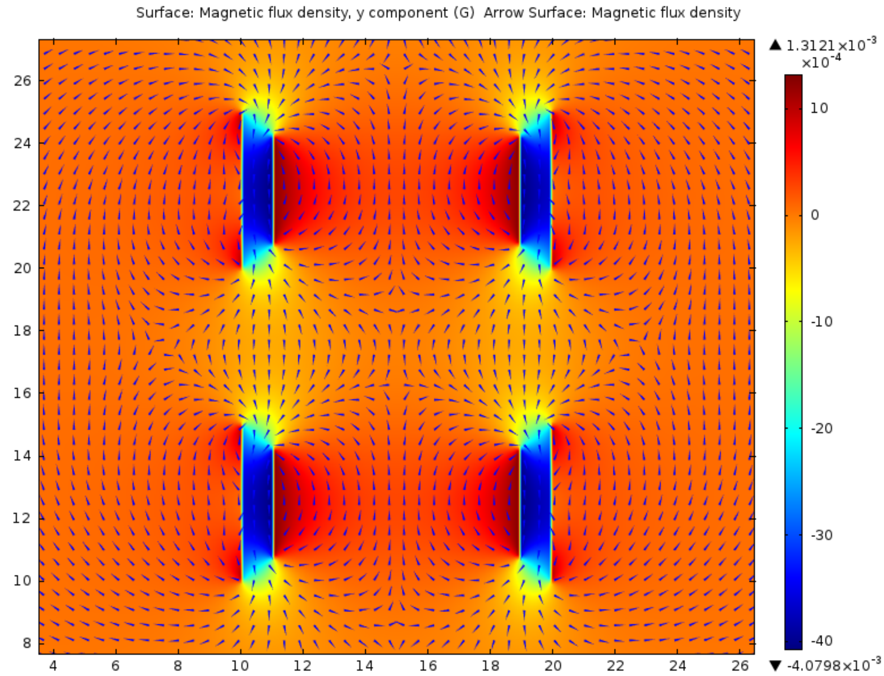

Figure 6.1: Simulation of the field inversion

6.2 Establishing the parasitic E-field

When deducing the magnetic fields components from the electric field probe the so labeled parasitic E-field due to the potentials on the inner conductors has to be considered (see page 41). Figure 6.2 shows the absolute electric field strength for variations around the z- and y-axis (15 cm arc length = central position). This figure has been generated with the model for the compact geometry with only electric potentials (0.75 V effective as in the measurement) applied to the inner conductors. From it the parasitic electric field strength of 0.4 V/m for each component at a misplacement of 3 mm has been deduced.

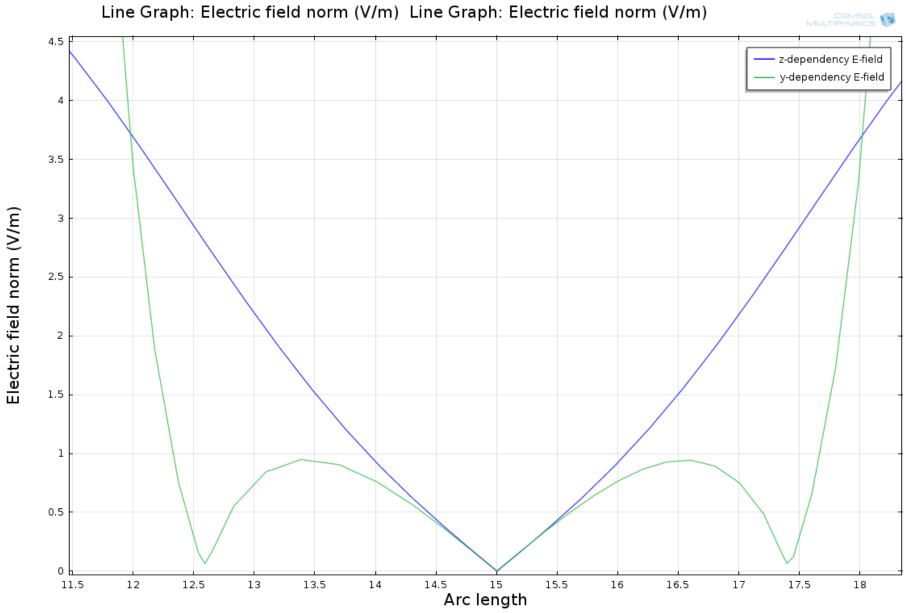

Figure 6.2: Simulation of the parasitic E-field

6.3 Reproducing the B_z vs. z dependency

Although the magnetic field probe has some systematic problems due to the antenna factor, it can still be used to measure the relative behaviour along the z-axis. From the field generated for the compact geometry wiring 1 in stripline mode at 1 MHz the B_z dependency on the position along the z-axis can be extracted (figure 6.3 a, green curve). This curve is rather flat in comparison to the DC expectation (orange curve) and the alternating field measurement. This changes for slight deviation from y=0 (other curves). On the actual field probe (for comparison see figure 5.11 b left) the tip, which likely contains the sensitive component, is 3 cm wide along the y-axis. So when comparing the simulation and the measurement this has to be taken into consideration.

Averaging over B_z z-dependencies from y=0 cm to y= 1.5 cm in the simulation (and scaling to best match the measurement point, compensate for the antenna factor uncertainty) yields the black curve in figure 6.3 b. The agreement between simulation and measurement (blue data points) is now far better than the original curve along y=0 alone. The asymmetry in the measurement is most likely induced by some ferromagnetic material in the laboratory.

6.4 Integral field from simulation

3D field simulations directly yield the integral fields on orbit (y=z=0 in the magnet coordinate system), when integrating the calculated field along this axis. But then assigning an error to these values is hardly possible. Though the simulations yield an error based on the deviations from iteration to iteration, this number can hardly be trusted as easily dominating systematic effects in the model are not considered. Accordingly no errors will be given on simulated values.

During the measurements with magnetic probes there was some doubt on the frequency dependent strength of the magnetic field. Simulation confirms that the strength is constant from 0.1 MHz to 1.5 MHz, as already indicated by the electric probe.

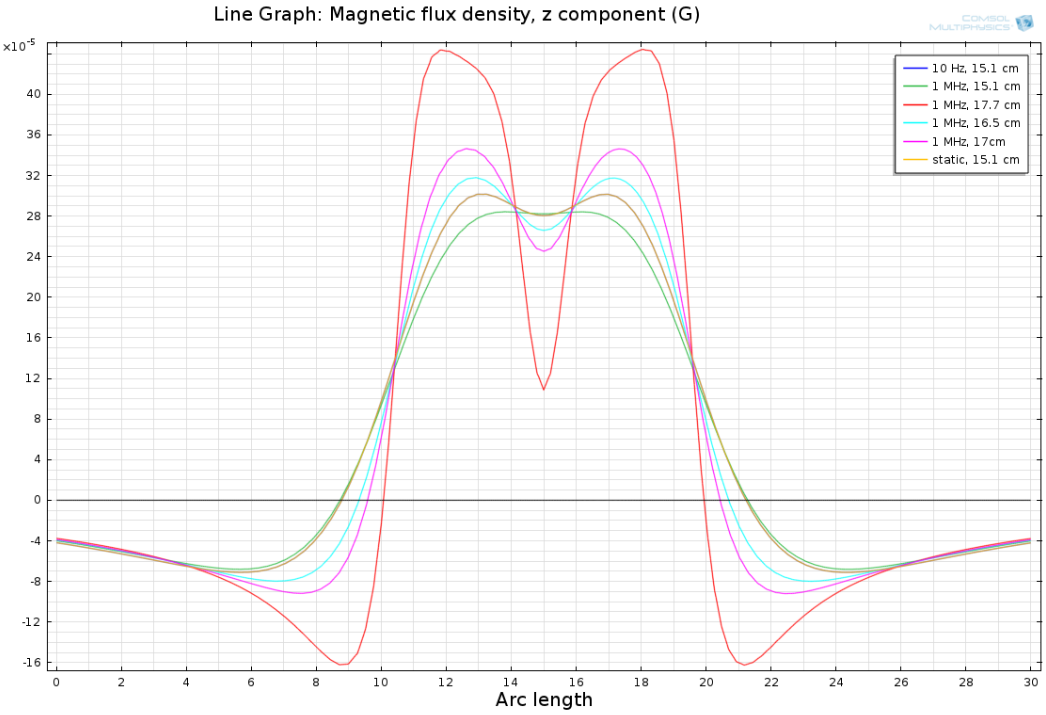

(a) B_z z-dependency at different y positions and frequencies

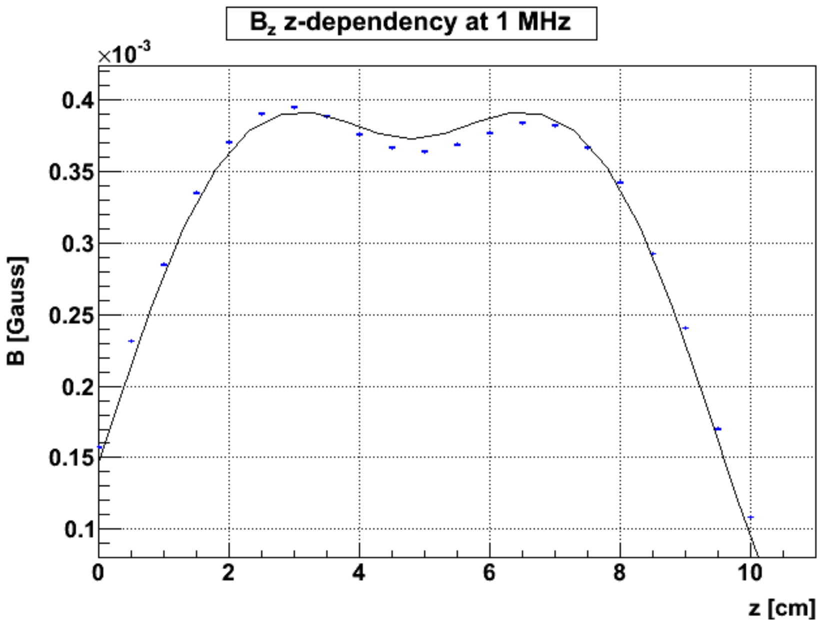

(b) B_z z-dependency for the probe as simulated and measured

Figure 6.3: Interpreting the B_z vs. z simulation

6.5 Integral fields by all accessible methods

Now that all methods have been presented it is time to compare the integral fields and to decide whether the magnet performs to specifications. This could be done for all available configurations, but as only wiring 1 in compact geometry has been in use at the accelerator, this summary will be limited to this scenario. Equivalent calculations for the other setups can be easily done with the numbers already presented.

The static and the alternating field measurements both do not directly yield integral fields but only deliver central field strength. For the DC measurement (classical mode) an effective magnet length and thus an integral field has already been determined from the fringe field behaviour (see page 36). For the alternating field measurement (stripline mode) this effective length is not necessarily the same, as the outer conductors are now additionally powered. In this case the effective length as seen in the 3D simulation (55 cm) can be used alternatively.

The alternating field measurement is of course not directly valid to describe the classical mode. Still an integral field can be deduced from this measurement when taking into account a conversion factor from stripline mode to classical mode as given by the simulation (roughly factor eight).

Combining numbers from different methods to calculate the integral field, although necessary, introduces a strong correlation between the different final results. Calculating a common average is thus not sensible. Below the final numbers at 200W are given in direct comparison:

6.5.1 Classical mode

method	$\int B\mathrm{dl}$ [Tmm]
alternating field meas. $\cdot$ simulated length $\cdot$ simulated factor:	0.023 ± 0.001 Tmm
static field measurement:	0.0240 ± 0.0007 Tmm
alternating field meas. $\cdot$ simulated length $\cdot$ factor:	0.023 ± 0.001 Tmm
3D DC simulation:	0.022 Tmm

6.5.2 Stripline mode

method	$\int B\mathrm{dl}$ [Tmm]
alternating field meas. $\cdot$ simulated length $\cdot$ simulated factor:	0.023 ± 0.001 Tmm
alternating field meas. $\cdot$ static length:	0.0031 ± 0.0002 Tmm
alternating field meas. $\cdot$ simulated length:	0.0028 ± 0.0001 Tmm
3D DC simulation:	0.0028 Tmm

All above values nicely agree within errors. For the classical mode the required integral field (0.025 Tmm) has already been reached, if the losslessness holds for the wiring in the accelerator (see section 7). For the systematically less problematic stripline mode an additional factor nine has to be achieved.

7 Results from the Froissart-Stora-Scans

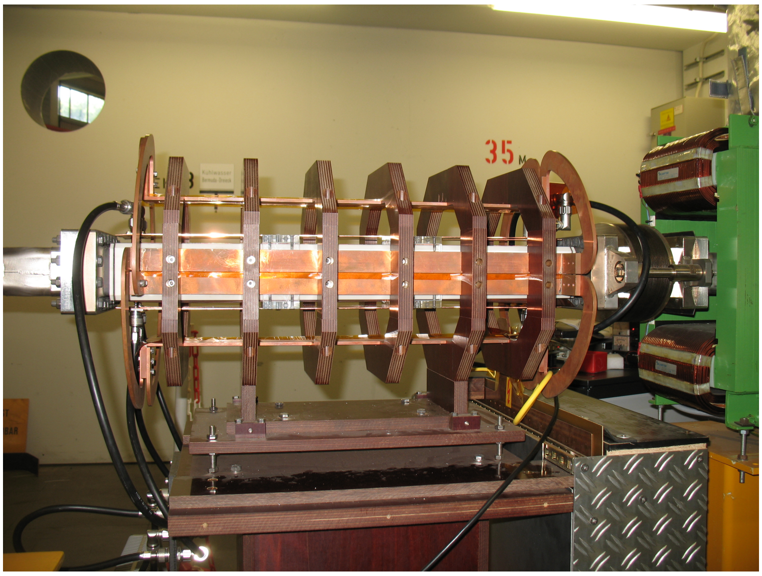

Figure 7.1: Stripline magnet at the COSY accelerator surrounded by a fast quadrupole

During the JEDI beamtime in May 2012 a couple of measurements with beam were performed to commission the new magnet. The main purpose of the beam-time was to investigate the effects of sextupole fields on the SCT [27]. This resulted in a cycle length of 80 s with deuterons at a momentum of 970 MeV/c at the time of the measurements.

The deuteron is composed of two fermions and is a spin 1 particle. From the relative abundance of the three possible vertical spin components $|+\rangle$, $|0\rangle$ and $|-\rangle$ the vector polarisation P_V and tensor polarisation P_T can be calculated as follows:

$$\begin{aligned} P_V &= \frac{N_+ - N_-}{N_+ + N_0 + N_-} \\ P_T &= 1 - \frac{3 \cdot N_0}{N_+ + N_0 + N_-} \end{aligned} \tag{7.1}$$

In the following only the vector polarisation is considered, as the FS-formula (see section 2.2.4) can then be used without modifications [28].

At first the magnet was wired in configuration 1 stripline mode and was operated at the spin resonace frequency, as previously measured by the solenoid. Only a 200 W amplifier was available, which only resulted in an obervable effect on the beam (coherent betatron oscillation), but not on the spin. The magnet was then rewired to match wiring 1 in classical mode (figure 7.2 shows how this can be achieved with the coaxial cable input) and a series of three FS-scans was performed.

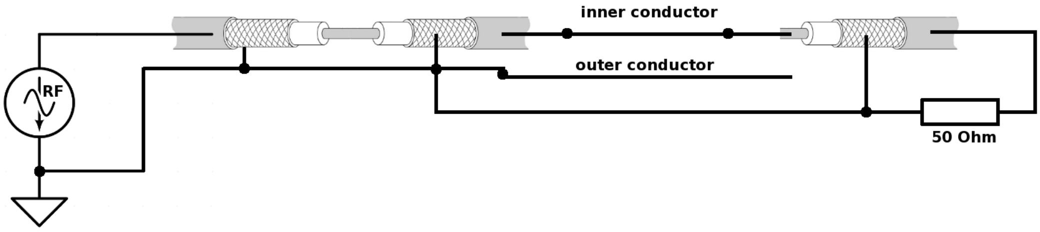

Figure 7.2: Circuit scheme to connect stripline to RF in wiring 1 classical mode

During all runs the time the magnet frequency was sweeped was constant at 67 s in order not to change the total cycle time of COSY. In order to achieve a strong polarisation change the ratio $\epsilon/(\Delta f/\Delta t)$ has to be high. Accordingly low Δf of 10 Hz (run 1207), 3 Hz (run 1208) and 0.9 Hz (run 1211) had to be chosen.

Figure 7.3 shows the evolution of the left-right asymmetry in the EDDA polarimeter in respect to the start point of EDDA data acquisition at the experimental energy, as recorded in run 1211 in 35 cycles. In order to convert to the actual beam polarisation one needs to consider the target and energy dependent analysing power of the polarimeter. Luckily we are only interested in ratios of polarisations, which are equivalent to the ratios of the directly accessible asymmetries.

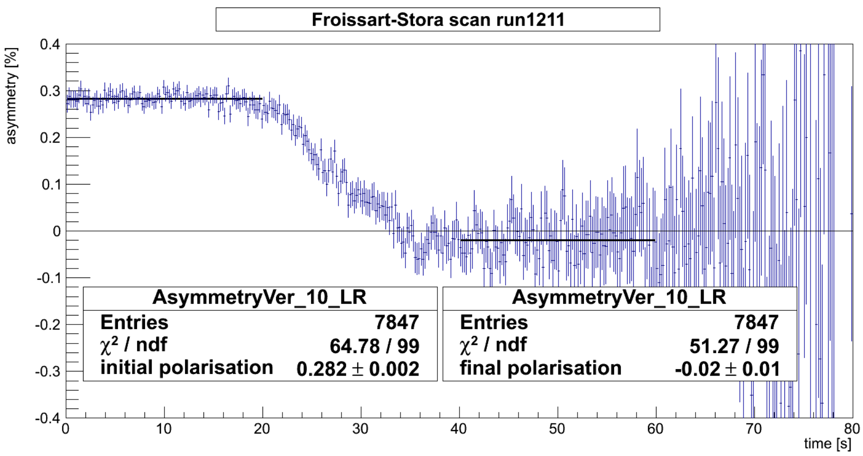

Figure 7.3: Evolution of the left-right asymmetry in the polarimeter over time ($\Delta f = 0.9Hz$)

From the initial and final asymmetry as well as the revolution frequency of the beam (750603 ± 1 Hz, from the cavity RF-amplifier) the effective resonance strength ϵ_{FS} in this run is calculated to be: $43.0 \pm 1.0 \cdot 10^{-9}$

The same has been done for the other two runs (see figure 9.1 and 9.2 in the appendix). The resulting resonance strengths were plotted against the frequency range (see figure 7.4) to check for any dependency as the FS conditions are more closely met. As expected the resonance strength decreases as Δf increases [14]. Based on the three data points it is not possible to deduce ϵ_{FS} for big frequency ranges, so that in the following the average effective resonance strength $\epsilon_{FS} = (39.5 \pm 0.9) \cdot 10^{-9}$ is considered.

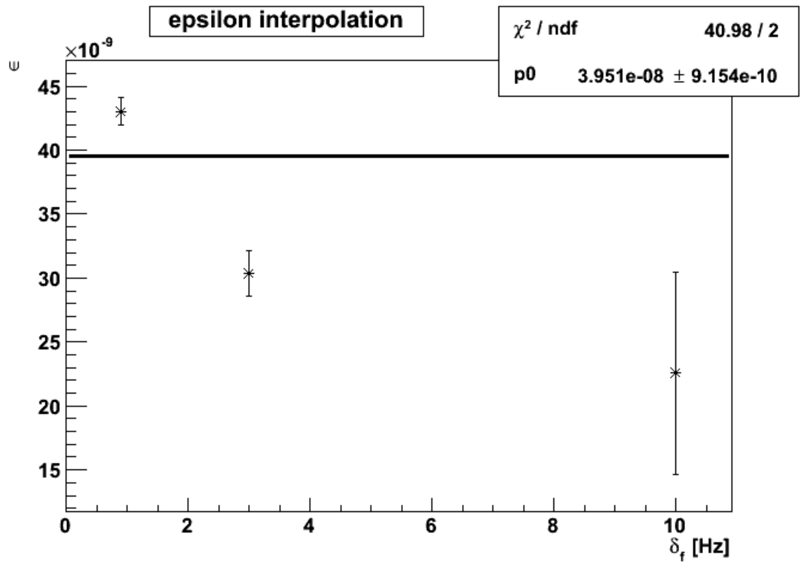

Figure 7.4: ϵ interpolation for all runs

This value is equivalent to an effective integral field as given by equation 2.22 of 0.00187 ± 0.00004 Tmm. Away from any intrinsic resonance this value has to be corrected at maximum by a factor 6.7, which would be equivalent to an integral field as seen in the laboratory of 0.0125 ± 0.0003 Tmm. Even this value is about a factor 2 away from the measured field strength (see section 6.5.1), which suggests that the FS-scans was not complete. The natural width of a resonance is given by $2 \cdot \epsilon \cdot f_c$ which for our case is around 0.9 Hz. The actual resonance width can easily be ten times bigger than this. In order for the FS-formula to be meaningful the frequency range has to be big compared to the resonance width. This condition is not fulfilled for any of the performed runs. Unfortunately larger frequency ranges were not possible without loosing the effect, because due to the limited time available at COSY the cycle time could not be increased.

8 Summary and Conclusions

A new RF dipole in stripline design has been presented and evaluated. The device has been designed to evaluate spin-rotation-systematics of a future EDM accelerator and is supposed to deliver an integral, radial field of 0.025 Tmm in a frequency range from 0.1 to 1.5 MHz.

The design of the magnet offers a great flexibility in both wiring scenarios and geometries. Any arbitrary waveform can easily be implemented as the magnet is constant in field strength over the considered frequency range..

In classical mode the desired field strength can already be reached at 200 W. In the systematically less critical stripline mode a factor nine has to be gained. Some weeks after the beamtime a 2000 W RF-amplifier has been repaired, which means that an additional factor three is already available without redesigning the magnet.

At about half the central field of the compact geometry the magnet can also be used in extended geometry to deliver comparably strong fields in both directions perpendicular to the beam.

These results were obtained through various measurements of static and alternating fields, as well as of simulations. The various methods agree well within the individual errors.

Concerning the method

Measurements of alternating magnetic fields at high frequencies are elaborate and strongly limited by systematics. At 1 MHz extrapolating from DC measurements and running simulations are good alternatives that yield results of comparable accuracy.

Commissioning with beam is essential to deduce the effective integral field at the specific accelerator conditions. Froissart-Stora scans offer a great and relatively simple way of doing so. Still in order to meet the FS conditions a number of parameters have to be optimised, which calls for a sufficiently long cycle, which could sadly not be delivered during the JEDI beamtime.

9 Appendix

Froissart-Stora-Scans

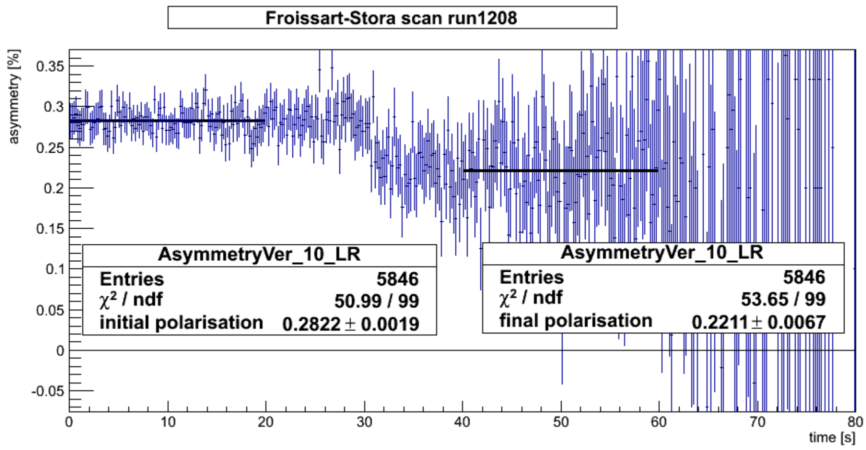

Figure 9.1: FS-scan run 1208 ($\Delta f = 3Hz$)

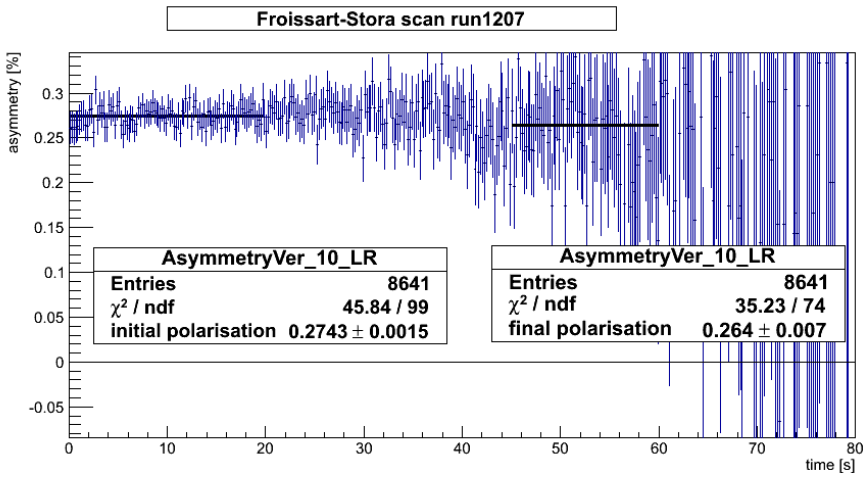

Figure 9.2: FS-scan run 1207 ($\Delta f = 10Hz$)

Static field measurement

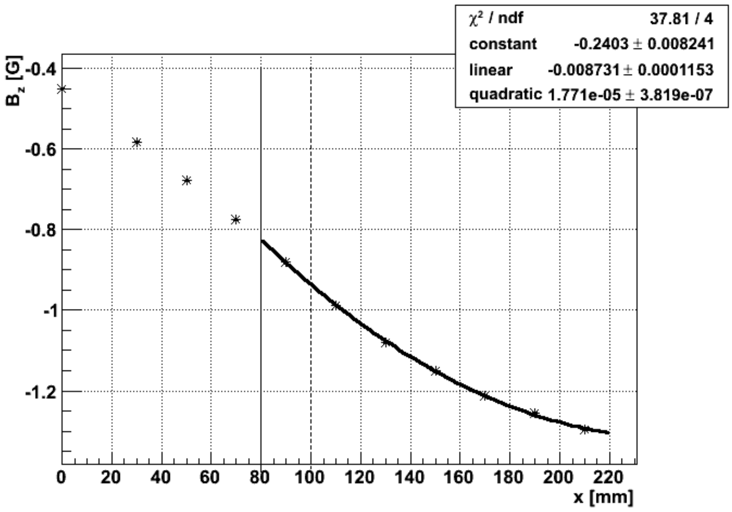

Figure 9.3: Fringe field behaviour at y = 150 mm

Alternating field measurements

see the following pages

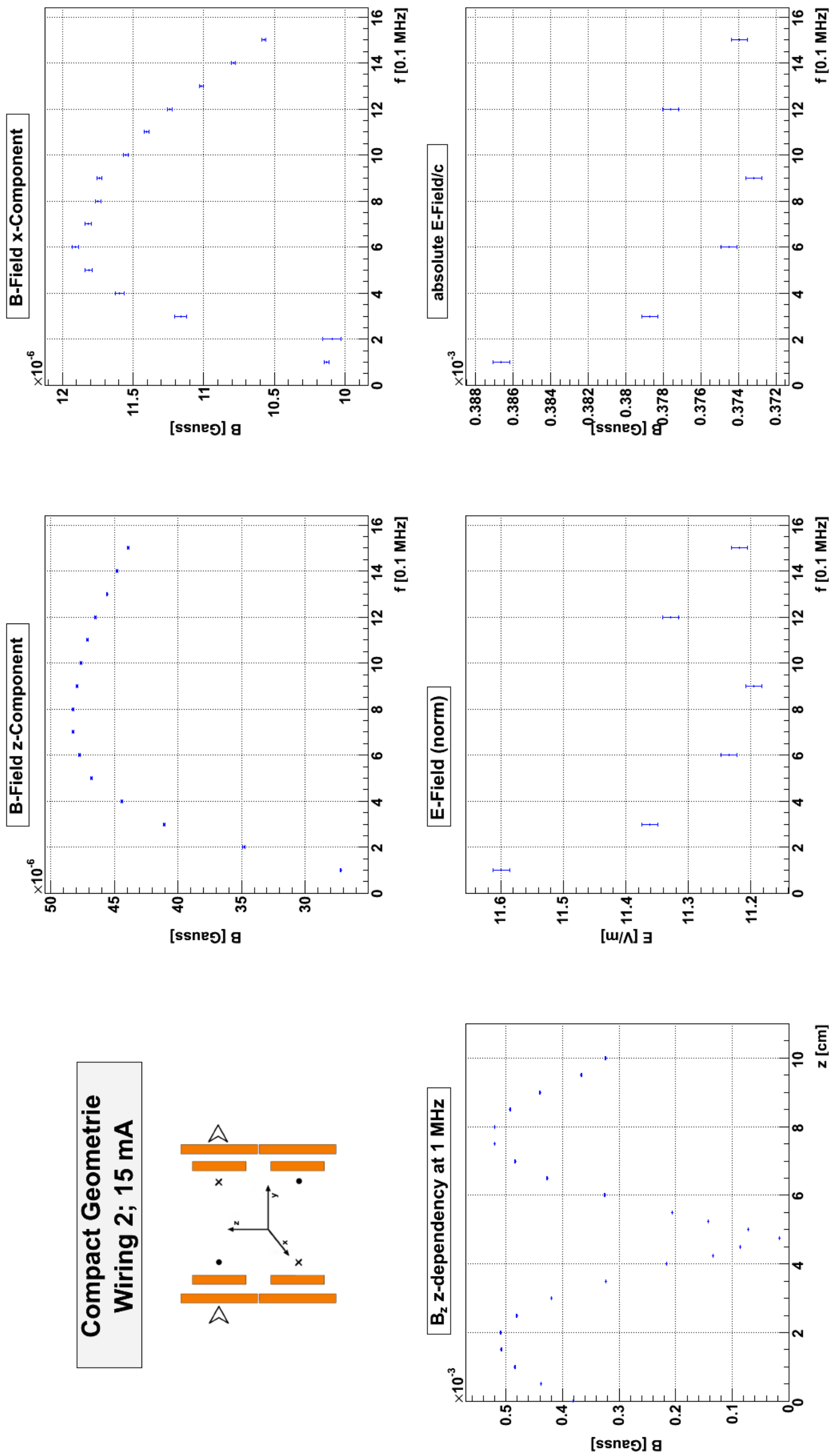

Figure 9.4: Compact geometry - Wiring 2

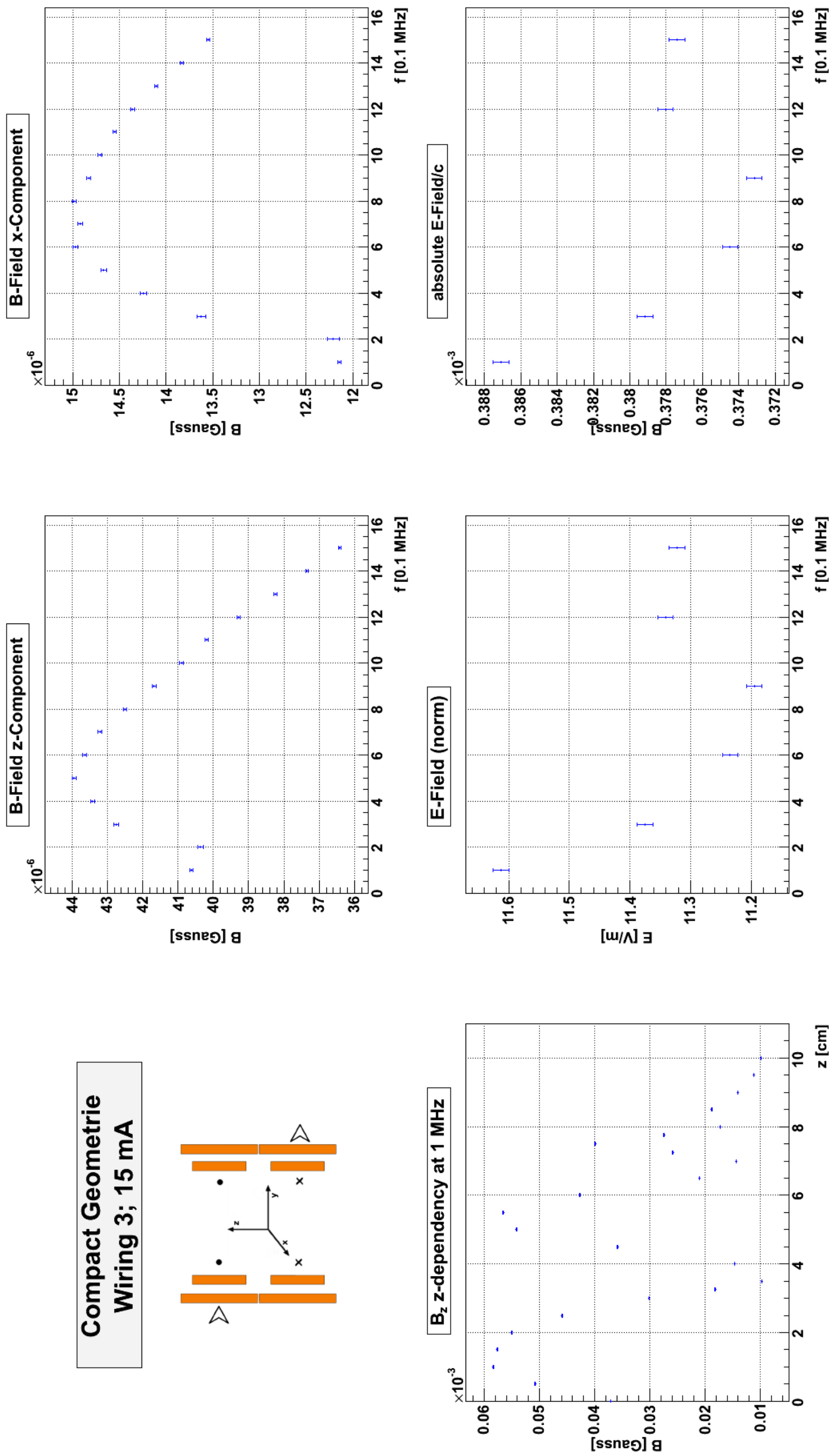

Figure 9.5: Compact geometry - Wiring 3

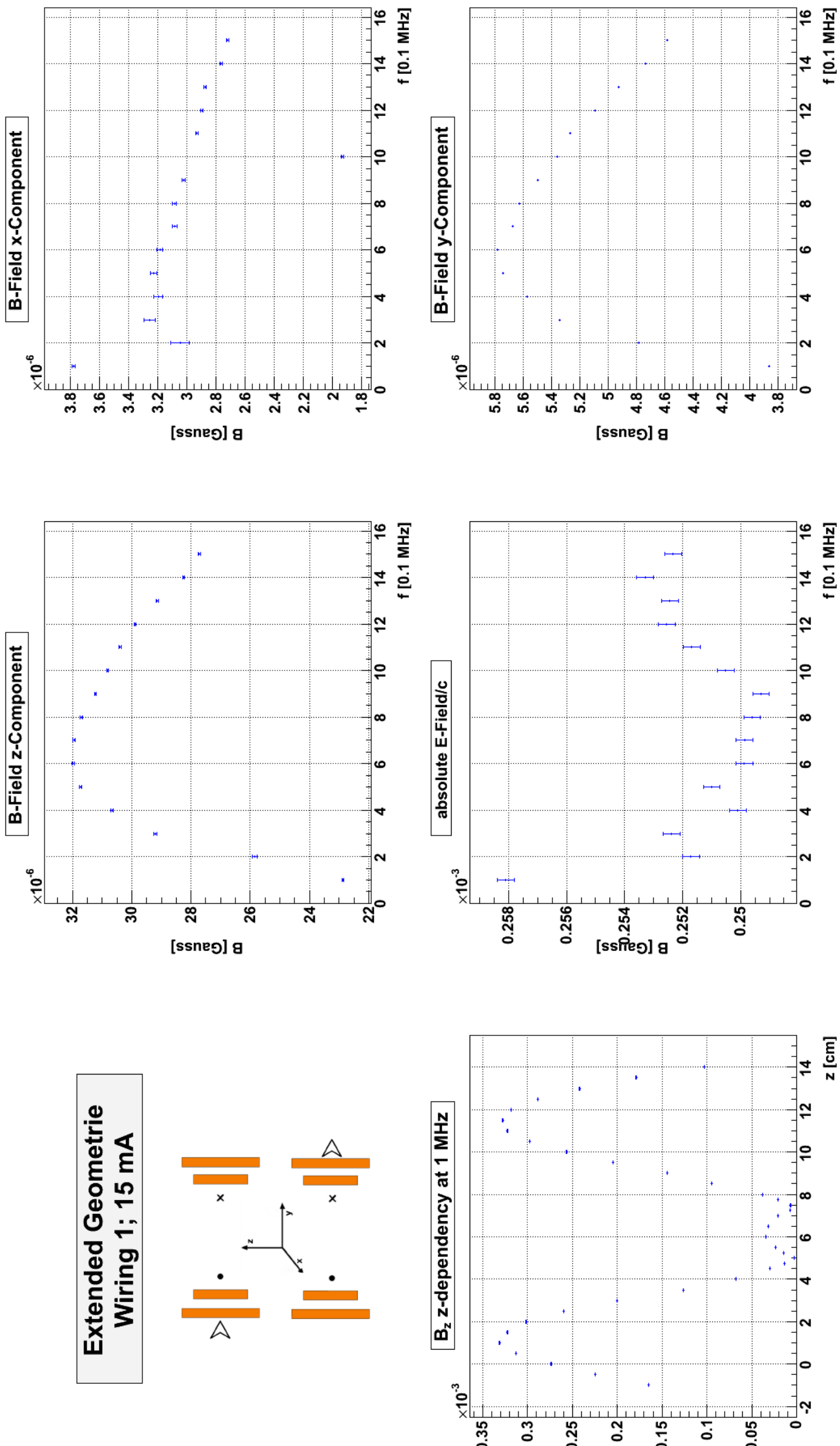

Figure 9.6: Extended geometry - Wiring 1

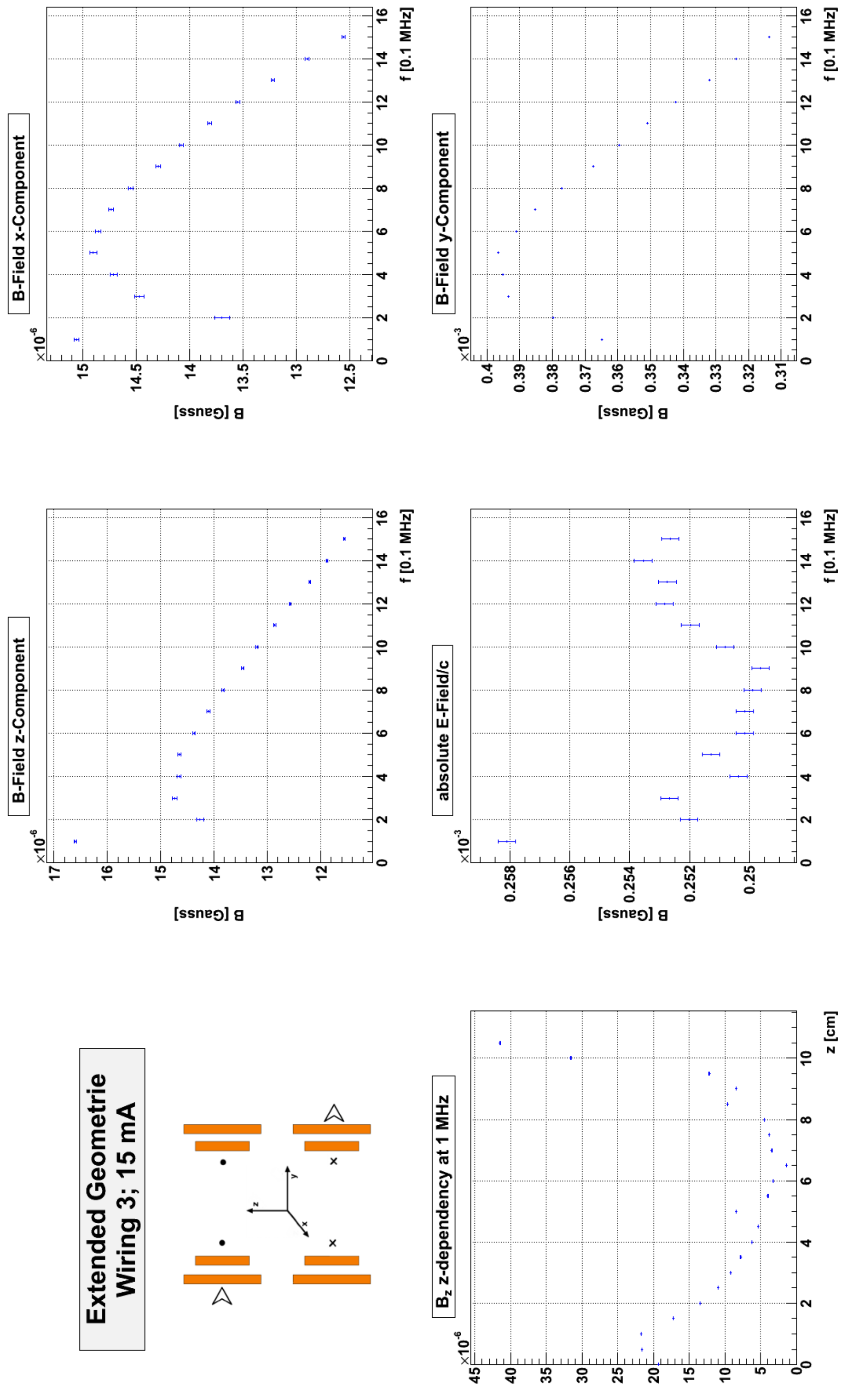

Figure 9.7: Extended geometry - Wiring 3

List of Figures

Bibliography

[1] JEDI collabortation, "Search for Permanent Electric Dipole Moments at COSY." Proposal, 2012.

[2] A. D. Sakharov, "Violation of CP invariance, C asymmetry, and baryon asymmetry of the universe," Journal of Experimental and Theoretical Physics, vol. 5, pp. 24–27, 1967.

[3] D. Spergel et al., "First year Wilkinson Microwave Anisotropy Probe (WMAP) observations: Determination of cosmological parameters," Astrophys.J.Suppl., vol. 148, pp. 175–194, 2003.

[4] J. H. Christenson, J. W. Cronin, V. L. Fitch, and R. Turlay, "Evidence for the 2π Decay of the K_2^0 Meson," Phys. Rev. Lett., vol. 13, pp. 138–140, Jul 1964.

[5] S. Chekmenev, "Review on current neutron EDM experiments." EDM seminar talk, 2012.

[6] Nikolaev, N., "Importance of Spin Coherence Time for EDM Searches." EDM seminar talk, 2012.

[7] C. Hanhart, "EDMs for light nuclei from the theoretical point of view: perspectives and potential." EDM seminar talk, 2012.

[8] K. Wille, Physik der Teilchenbeschleuniger und Synchrotronstrahlungsquellen. Teubner Studienbücher, Teubner, 1992.

[9] "The American Heritage Dictionary of the English Language," 2010. Houghton Mifflin Harcourt Publishing Company.

[10] The Wakasa Wan Energy Research Center. http://www.werc.or.jp/english/reseadeve/activities/accelerator/accelerator/synchro/index.htm.

[11] Lehrach, A., Strahl- und Spindynamik von Hadronenstrahlen in Mittelenergie-Ringbeschleunigern. Forschungszentrum Jülich, 2008.

[12] A. Lehrach, "Accelerator related issues for storage ring EDM searches." EDM seminar talk, 2012.

[13] Goslaski, P., "Hochpräzise Impulsbestimmung des COSY-Beschleunigerstrahls im Rahmen der Messung zur Bestimmung der μ-Masse am Experimentaufbau ANKE," 2008.

[14] A. Lehrach, "Private communication." June 2012.

[15] M. Froissart and R. Stora, "Depolarisation d'un faisceau de protons polarises dans un synchrotron." http://www.sciencedirect.com/science/article/pii/0029554X60900331, 1960.

[16] Krisch, A. D., Leonova, M. A., Gebel, R., Lehrach, A., Lorentz, B., Maier, R., Prasuhn, D., Schnase, A., Stockhorst, H. and others, "Unexpected reduction of rf spin resonance strength for stored deuteron beams." http://link.aps.org/doi/10.1103/PhysRevSTAB.10.071001, Jul 2007.

[17] R. Talman , Cornell University, Ithaca, N.Y., "All-In-One Storage Ring Lattice for Baryon EDM Measurements." February, 2012.

[18] R. Talman, "Storage rings for electric dipole measurements." EDM seminar talk, 2012.

[19] L. P. Stephenson E.J. et al., "Studies of the Horizontal Spin Coherence Lifetime." COSY Beam Time Request (176.6), 2012.

[20] Grzonka, D., "Transnational Access to COSY-Jülich," 2010. HadronPhysics2 MidTerm review.

[21] R. Gebel, "Private communication." June 2012.

[22] Garcia, I.R., Calculation methodology and fabrication procedures for particle accelerator strip-line kickers: Application to the CTF3 Combiner Ring extraction kicker and TL2 tail clippers. PhD thesis, Universidad Politécnica de Madrid, 2009.

[23] Three-axis Hall Magnetometer THM1176. Metrolab Technology SA Switzerland, 2012.

[24] "R&S ESU EMI Test Receiver Operating Manual." http://www.rohde-schwarz.de/file/ESU˙Operating˙Manual˙English˙FW4.43.pdf, 2009.

[25] "R&S HZ-14 Probe Set for E and H Near-Field Measurements Operating Manual." http://www.rohde-schwarz.de/file/HZ-14˙e˙1-1.pdf, 2011.

[26] Cookbook for EMC Precompliance Measurements. Hewlett Packert, 1997.

[27] Stephenson E.J. et al, "Synchrotron oscillation effects on an RF-solenoid spin resonance." Draft version.

[28] Leonova, M.A., "SPINatCOSY: Spin-Manipulating Polarized Deuterons and Protons," 2008.